SIMILAR AND DISSIMILAR FRICTION STIR WELDING OF NICKEL-TITANIUM SHAPE MEMORY ALLOYS

A Thesis

by

PARKER HAMILTON WEST

Submitted to the Office of Graduate and Professional Studies of
Texas A&M University
in partial fulfillment of the requirements for the degree of

MASTER OF SCIENCE

Chair of Committee,	Bilal Mansoor
Committee Members,	Ibrahim Karaman
	Arun Srinivasa
Head of Department,	Andreas Polycarpou

August 2018

Major Subject: Mechanical Engineering

ABSTRACT

The feasibility of using friction stir welding (FSW) to join nickel-titanium (NiTi) shape memory alloys (SMAs), both to themselves and to other materials, has been explored. The effects of the FSW process on the microstructure, mechanical properties, and shape memory effect have been investigated. The results indicate that friction stir welding is a suitable method for similar welding of NiTi SMAs, giving a joint efficiency of 93% when the NiTi was tested in its martensitic phase, and a joint efficiency of 84% at elevated temperatures, with the NiTi in its austenite phase. In both cases, fracture was observed to be of a ductile nature. Due to the grain refinement experienced in the stir zone (SZ) of the weld, the material in this region showed more strain hardening than the base metal. The martensitic plateau characteristic of SMAs when tested in their martensitic phase was observed in the welded region, indicating that detwinning is still the dominant mode of martensite deformation at low strains, even within the weld itself. The transformation temperatures within the stir zone, measured by differential scanning calorimetry (DSC), showed little to no change when compared to the base metal. Significant scatter was seen in the microhardness values measured on the cross section of the weld, even at distances far from the weld. Finely dispersed tungsten particles of about 75 nm were seen deposited in some welds, a result of tool wear.

FSW of NiTi to Inconel 625 and Ti-6Al-4V proved difficult, but dissimilar welds between NiTi and 304 stainless steel were achieved, with a joint efficiency of 80% at room temperature and 100% at high temperatures, when the NiTi was in its austenite

phase. Additionally, the use of a permanent stainless steel backing strip resulted in a joint efficiency of 100% even at low temperatures, when the NiTi was martensite. The SZ was found to consist of refined grains averaging 8 μm in size, compared to 20 μm in the stir zone of the NiTi similar welds. Although welding parameters were not optimized for steady-state defect-free welds, defect-free sections were produced in the transient portion of the weld.

DEDICATION

This thesis is dedicated to my wife and parents:

To my mother, for being actively involved with my education and maintaining high expectations.

To my father, for teaching 5 year-old Parker how to weld, letting me "help" in the garage, and giving me a love of designing and building things. You really gave me a jump-start on engineering.

To my beautiful wife, Jenny, for marrying me before I had a full-time job, for traveling all over the world with me (and always knowing what to do when we arrive), and for supporting me, even through late nights in the lab. You make everything more enjoyable.

ACKNOWLEDGEMENTS

I would like to thank my committee chair, Dr. Mansoor, and my committee members, Dr. Karaman and Dr. Srinivasa, for supporting and facilitating my research, and for providing feedback as my work progressed.

Thanks also to the staff and fellow students at Texas A&M University, both in College Station and Qatar, for teaching me how to work in a lab, for getting parts machined in a time crunch, and for providing feedback on my ideas, both good and bad.

Finally, I would like to thank my parents for their encouragement and support of my education, and my wife for her love and patience, and her assistance in the lab.

CONTRIBUTORS AND FUNDING SOURCES

This work was completed under the supervision of a thesis committee chaired by Dr. Bilal Mansoor, Department of Mechanical Engineering, and committee members Dr. Ibrahim Karaman of the Department of Materials Science and Engineering and Dr. Arun Srinivasa of the Department of Mechanical Engineering. All work for the thesis was conducted by the student under the advice of Dr. Mansoor and Dr. Karaman.

Graduate study was supported by startup and discretionary funds from Dr. Mansoor, as well as a fellowship from Texas A&M University.

TABLE OF CONTENTS

Page

LIST OF FIGURES

Page

LIST OF TABLES

Page

CHAPTER I

INTRODUCTION AND LITERATURE REVIEW

Shape memory alloys (SMAs) are a special class of materials that have the ability to “remember” their original shapes after experiencing plastic deformation. When plastically strained at low temperatures and then heated, a SMA will undergo a phase transformation and revert to its former shape. Shape memory alloys consisting of a near-equiatomic nickel-titanium (NiTi) mixture were discovered in 1961 [1], but their implementation has been retarded by a few challenges. One of the biggest challenges faced when working with SMAs is the lack of effective methods to join them, both to themselves and to other materials [2]. The methods used have ranged from mechanically fastening to adhesive bonding to brazing, and each method has its own advantages and drawbacks. Welding of SMAs is technologically significant as it offers the possibility of reducing weight without compromising on strength in welded joints compared to other fastening approaches, but welding NiTi SMAs to themselves has proven difficult enough, and welding NiTi to dissimilar alloys is even more problematic.

An early attempt to weld NiTi using the tungsten inert gas (TIG) process resulted in the formation of a relatively large heat affected zone (HAZ) that was much weaker than the base metal, and a low ultimate tensile strength (UTS) of 267 MPa [3]. Due to the relatively large HAZ associated with TIG welding, most recent studies have focused on laser welding [4]. Falvo et al [5] reported that nickel-rich NiTi welded with a neodymium-doped yttrium aluminum garnet (Nd:YAG) laser displayed a UTS of 520 MPa at an elongation to failure of 7%. When compared to the base metal, which had a

UTS of 1100 MPa, this translates to a weld efficiency of 47%. The transformation temperatures were seen to increase, with the austenite finish (A_f) temperature increasing by 23°C. Additionally, the weld showed an increase in irrecoverable strain (ε_{irr}) when compared to the base metal.

The relatively low strength seen in NiTi joints produced by laser and TIG welding stems from the fact that these methods involve the melting and resolidification of the workpiece material. In general, fusion welding techniques have many drawbacks when it comes to welding NiTi. One such drawback is simply that the material will typically take on a coarse-grained cast microstructure as the melt pool solidifies, reducing the strength and shape memory abilities of the material [6]. Additionally, the transformation temperatures of NiTi SMAs are very sensitive to composition. Even a 1 at% change in the nickel content of the alloy can result in a shift of transformation temperatures of approximately 100°C [7]. In fusion welding processes, the temperatures in the weld pool can cause small amounts of nickel to vaporize, resulting in a large shift in transformation temperatures that complicates the use of the shape memory effect.

Explosive welding was the first successful method of welding NiTi to dissimilar metals [8], but in addition to being limited to lap joints, explosive welding is plagued with noise issues, high costs, and paperwork associated with the transportation and storage of explosives [9]. The most researched method to-date for welding NiTi to dissimilar metals is laser welding [4]. However, brittle intermetallic compounds tend to form in the melt pool, and the hardness of the weld is seen to double when compared to the hardness of the base metals [10]. Since all fusion welding processes involve the melting and resolidification of the materials, there tends to be substantial diffusion between them, resulting in the growth of undesirable intermetallic phases such as Ti_2Ni and $TiNi_3$, as seen in Figure 1.

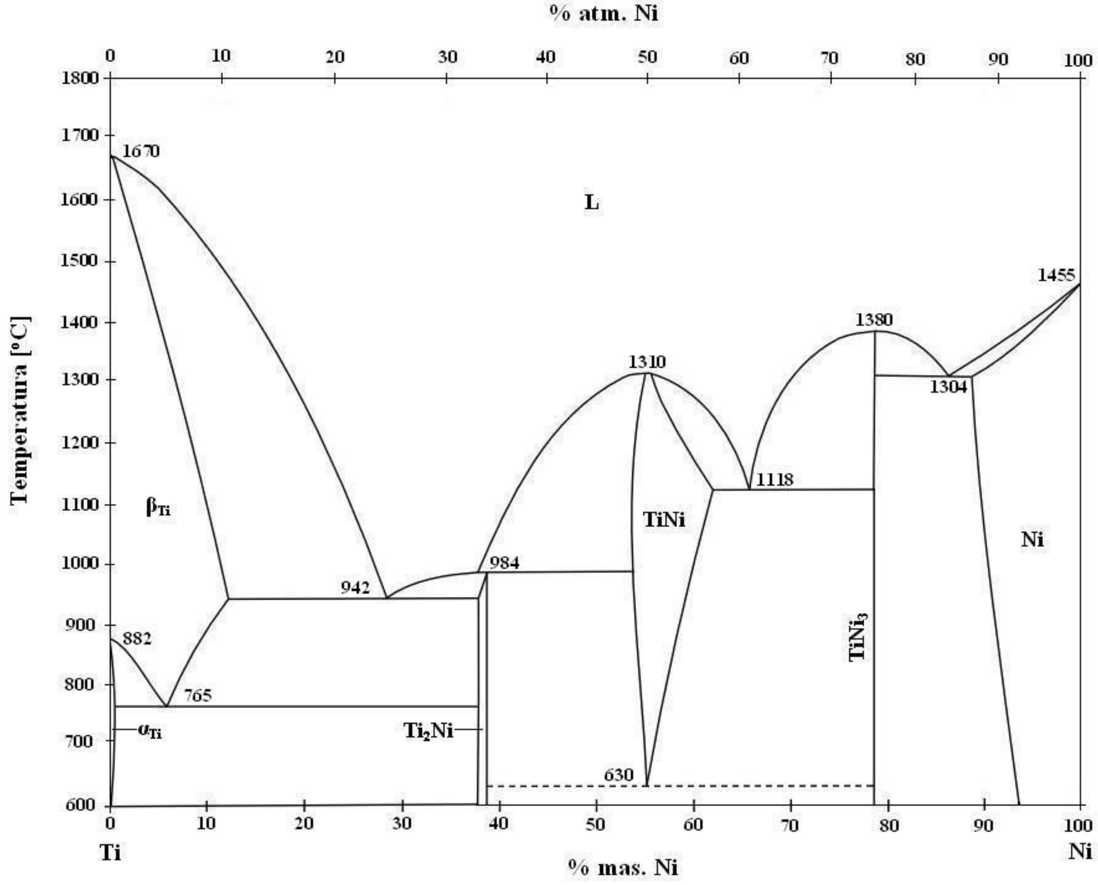

Figure 1: The Ni-Ti system phase diagram, reprinted from [11].

One way to limit the growth of these brittle intermetallic compounds is to avoid ever melting the materials. The diffusion rates seen at solid-solid interfaces, even at very high temperatures, are still much lower than those seen in liquid-liquid interfaces, which may limit the growth of such undesirable phases. Additionally, if these thin intermetallic layers can be broken up by mechanical processes and dispersed as fine particles throughout the weld, they are much less likely to act as crack initiation sites. Since friction stir welding is a solid-state process that vigorously mixes the weld material, it poses as an effective method of welding NiTi to dissimilar metals.

Friction stir welding is a relatively new solid-state welding process that consists of a rotating tool translating along a joint, as illustrated in Figure 2. The friction of the shoulder rubbing on the workpiece generates heat and softens the workpieces, while the rotating pin stirs the two workpieces together [12].

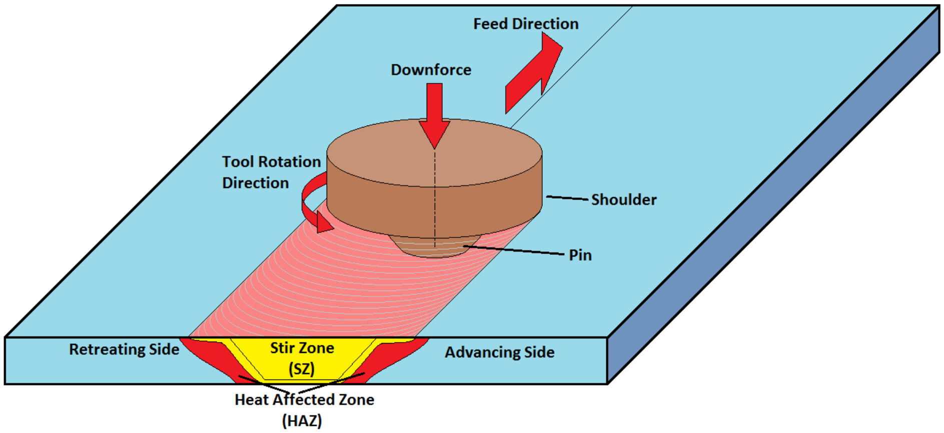

Figure 2: A schematic illustration of the friction stir welding process.

The temperatures generated in the process are typically around 80% of the melting point of the metal [13], and FSW, a severe plastic deformation process, results in significant grain refinement in the weld zone. This stands in contrast to fusion welding techniques, which tend to form a cast microstructure in the fusion zone [6]. Since FSW lacks many of the drawbacks associated with fusion welding processes, it appears as a promising method of welding SMAs.

To the best of our knowledge, to date two studies [14, 15] have been published in open literature on similar FSW of NiTi SMAs; however, none have been conducted on FSW of martensitic NiTi, meaning NiTi that is in its low temperature (martensite) phase at room temperature. Two additional studies in existing literature have focused on friction stir processing (FSP) of NiTi [16, 17]. FSP is the bead-on-plate equivalent of FSW, where a rotating tool is driven through just one workpiece, rather than along the joint between two workpieces. Although not a true welding process, FSP can be used to optimize the processing parameters that can then be applied in FSW. FSP is typically done to learn about the impact of FSW on the microstructure of a workpiece and to understand the role that reduction in the grain size in processed areas can have on the mechanical properties. A summary of these studies from open literature is presented in Table 1.

Table 1: A summary of FSW/FSP of NiTi results available in literature.

Study	Tool Material and Geometry	FSW Parameters	Outcomes
FSP of 6.35 mm Austenitic NiTi 2005 [16]	Densimet shoulder Ø24.1 mm, W-Re threaded pin Ø7.9 mm, 5.84 mm long	Rotation – 600 rpm Feed Rate – 12.7 mm/min	Welded and hot rolled UTS = 650 MPa at 16% strain vs 630 MPa in BM. A_f dropped from 15°C (BM) to -23°C (Weld) Grain refinement from 45 µm (BM) to 27 µm (Weld)
FSP of 0.5 mm Martensitic NiTi [17]	W-alloy shoulderless tool, Ø3.6 mm at tip, 45° taper	Rotation – 500 rpm Feed Rate – 50 mm/min	Strength not tested A_f increased from 100°C (BM) to 120°C (measured by bending test)
FSW of 1.2 mm Austenitic NiTi [14]	Densimet W-alloy, shoulder Ø22 mm, pin Ø5 mm, 0.9 mm long	Rotation – 1000 rpm Feed Rate – 50 mm/min Tool Tilt – 2°	UTS of 638 MPa (Weld) at 4-7.5% strain vs. 965 MPa (BM). Hardness decreased from 277 HV (BM) to 262 HV (Weld), with scatter of +/- 10 HV A_f decreased from 9°C (BM) to -7°C (Weld)
FSW of "thin" Austenitic NiTi [15]	Unknown material, shoulder Ø17 mm, pin Ø2 mm at tip, unknown length	Rotation – 1500 rpm Feed Rate – 180 mm/min	Weld UTS of 700 MPa at 13% strain, BM UTS unknown. Hardness increased from 340 HV to 355 HV, with a scatter of +/- 10 HV in the weld, and +/- 3 HV outside of the weld zone

Only one of these studies was focused on martensitic NiTi. However, in that study the mechanical properties of the resulting joints were not investigated [17]. Since martensitic NiTi is used in actuators in the automotive and aerospace industries [18], it is important that the effects of FSW/FSP on the strength and shape memory response of martensitic NiTi are well understood. Therefore, the first goal of this study is to explore the potential of applying FSW to NiTi SMAs, and obtain good quality butt welds. The key objectives include understanding the effects of FSW on, (i) the transformation temperatures, and, (ii) both the ambient temperature (martensite) and high temperature (austenite) mechanical response of NiTi.

Although there have been numerous documented attempts at laser welding NiTi to dissimilar metals, there exist no studies in published literature on successfully friction stir welding NiTi to dissimilar materials. A 2007 investigation into methods of joining NiTi to Ti-6Al-4V touched upon using friction stir spot welding (FSSW), a derivative of FSW, for this purpose; however, the attempts at spot welding NiTi to Ti-6Al-4V using this method were deemed unsuccessful and abandoned in favor of other methods [19]. Therefore, the second goal of this study is to explore the potential of using FSW to join NiTi to dissimilar metals, namely Inconel 625, Ti-6Al-4V, and AISI 304 stainless steel. The chemical, mechanical, and thermal properties of all of these alloys can be seen in Table 2.

Table 2: Material properties (Adapted from mill test reports, [20], [21]).

Material	NiTi, Equiatomic	Ti-6Al-4V	Inconel 625	304 Stainless Steel
Density, kg/m^3	6500	4430	8440	8000
Primary Constituents, at%	Ni-50% Ti-50%	Ti-86% Al-10%	Ni-62% Cr-25%	Fe-72% Cr-18% Ni-8%
Melting Point, °C	1275	1604	1290	1400
Thermal Conductivity, W/m*K	19	6.7	9.8	16.2
Heat Capacity, kJ/kg*K	0.5	0.6	0.41	0.5
Thermal Diffusivity, mm^2/s	4 6	2.5	2.8	4.1
UTS at room temp (MPa)	900	950	880	750
UTS at 600 C (MPa)	180 (Interpolated)	325	760	250

Among the selected alloys for dissimilar welding, Ti-6Al-4V and 304 stainless steel offer good biocompatibility and are used in conjunction with NiTi in the biomedical industry, as well as in the aerospace industry. Inconel 625, a nickel-based superalloy, is also renowned for its corrosion resistance and strength even in high temperature environments such as jet engine nozzles.

Using these three alloys allows conclusions to be drawn about the feasibility of welding NiTi to titanium-based alloys, nickel-based alloys, and iron-based alloys in general. The key objectives of this portion of the study include understanding the effect of the FSW process on the transformation temperatures of the NiTi after welding with dissimilar materials, and the mechanical properties of the joint at room temperature and high temperatures.

CHAPTER II

SIMILAR FRICTION STIR WELDING OF NiTi

The first half of this study focuses on friction stir welding of NiTi to itself, and the resulting effects on the microstructure, mechanical properties, and shape memory effect.

Experimental

The materials and methods used for performing and characterizing the NiTi-NiTi welds are detailed below.

Materials

In this study, 2 mm sheets of nominally equiatomic NiTi were cut by Electrical Discharge Machining (EDM) as slabs off of a large extruded bar, as seen in Figure 3. Each of these slabs was then cut into two welding coupons, as can be seen in Figure 4.

Figure 3: A segment of the original NiTi extruded bar.

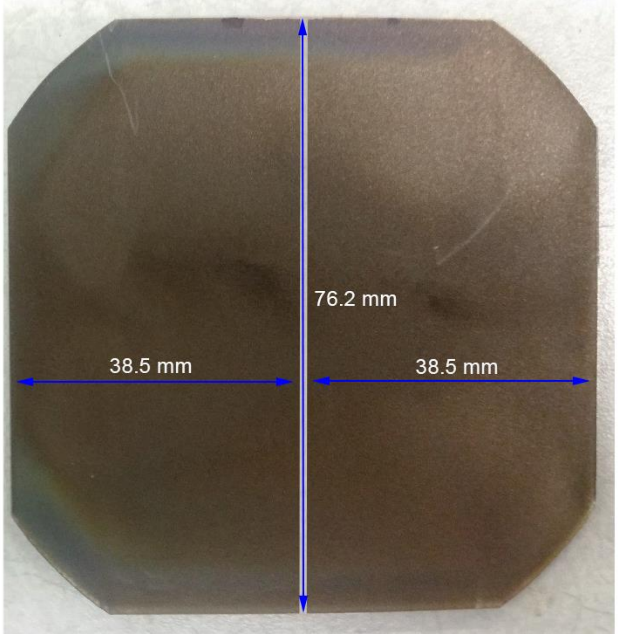

Figure 4: Sheets cut from NiTi bar, used as welding coupons in this study.

The grain structure of the original NiTi bar was typical of extruded bars, with grains elongated in the direction of extrusion. This can be seen in Figure 5, a view of the cross-section of one of the 2 mm thick sheets that was cut from the bar.

Figure 5: A collage of low-magnification optical microscopy images, revealing the overall microstructure of the original NiTi shape memory alloy.

Friction Stir Welding Process

Friction stir welding was carried out on 38.5 mm x 76.2 mm (length x width) welding coupons, 2 mm thick. The NiTi sheets were lightly sanded prior to welding to remove the EDM recast layer. Welds were then performed at three different spindle speeds. The parameters chosen for the welds were based off of the optimal parameters reported for FSW of 2 mm thick Ti-6Al-4V sheets using a tool of similar geometry [22]. The test matrix can be seen in Table 3.

Table 3: The friction stir welding test matrix applied in this study

Weld	Feed Rate (mm/min)	Spindle Speed (rpm)	Tool Tilt (deg)
1.	75	350	2.5°
2.	75	400	2.5°
3.	75	450	2.5°

The tool used was made of a tungsten-rhenium (W-Re) alloy, with a 15 mm diameter shoulder. Tungsten-rhenium displays excellent strength at high temperatures [23], and has been successfully used in a number of studies on FSW of titanium alloys [22, 24]. As depicted in Figure 6, the 1.7 mm long pin was in the shape of a frustum, or a truncated cone, tapering from 9 mm in diameter to 5 mm in diameter.

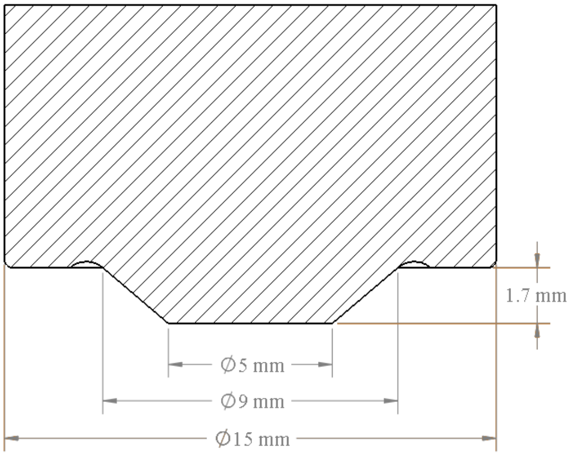

Figure 6: The geometry of the tool used in this friction stir welding study.

The two pieces of NiTi to be welded were clamped to an 8 mm thick manganese steel backing plate in the manner shown in Figure 7.

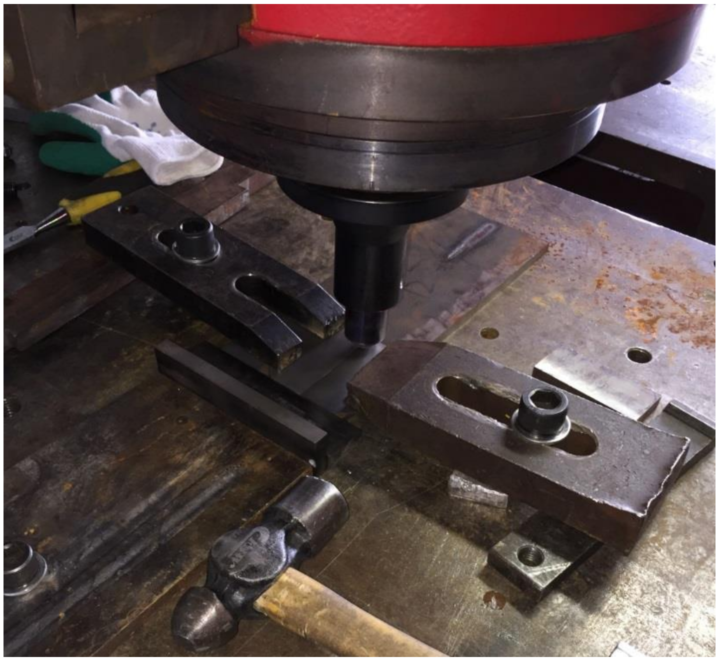

Figure 7: Fixturing of NiTi sheets prior to the start of welding.

The tool tilt angle was 2.5° for all welds. The welding process was initiated by plunging the spinning tool into the workpieces at a rate of 5 mm/min. After the full plunge depth had been reached, the tool was driven forward along the joint at 75 mm/min. Once the tool had reached the end of the weld, it was allowed to dwell there for 1 second, before being retracted at 10 mm/min. The then-welded workpiece was allowed to cool before being removed from the backing plate. It was difficult to remove the samples from the backing plate, as they had become welded to it. This caused problems that were discovered when characterizing the welds, as a streak of iron was drawn up into the weld zone. The welding process was then completed for the remainder of the welds in the matrix, using different welding parameters.

After a preliminary set of tests was performed on these welds, a second weld was made with a spindle speed of 400 rpm. To avoid the problems encountered in the first batch of welds when the workpieces were welded to the backing plate and iron from the steel backing plate was drawn up into the weld, the workpieces for this weld were placed over a small NiTi backing strip. When this weld was completed, the backing strip was not pried away. Rather, it was machined off for further analysis. This final weld was then subjected to more in-depth characterization. Tensile and DSC samples were cut from each welded sample, as well as from the base metal. Unless otherwise noted, results presented are from the final weld at 400 rpm. To further explore the processing parameter envelope of NiTi, two additional sheets of NiTi were subjected to friction stir processing (FSP) using spindle speeds of 300 and 500 rpm.

Differential Scanning Calorimetry

After the welds were performed, differential scanning calorimetry (DSC) samples, 3 mm in diameter and 1.5 mm tall, were cut at regular intervals across the cross section of the welds. Three DSC cycles were then run at a heating and cooling rate of 10°C per minute. The first DSC sample to be run was taken from the very middle of the weld, where the maximum change in transformation temperatures was expected to be seen. It was cooled to -150°C and heated to 150°C for each cycle. After it was seen that there was no transformation below 40°C, the minimum temperature for the DSC testing of the remaining samples was changed to -50°C. Two DSC samples were also cut from the base metal. The results from these two samples not only served as a control to compare the welded samples to, but also gave an idea as to the amount of random scatter to be expected in DSC curves.

Tensile Tests

Tensile tests were conducted on both the welded samples and the base metal specimens. Tensile specimens of the welded samples were cut perpendicular to the weld according to the dimensions in Figure 8.

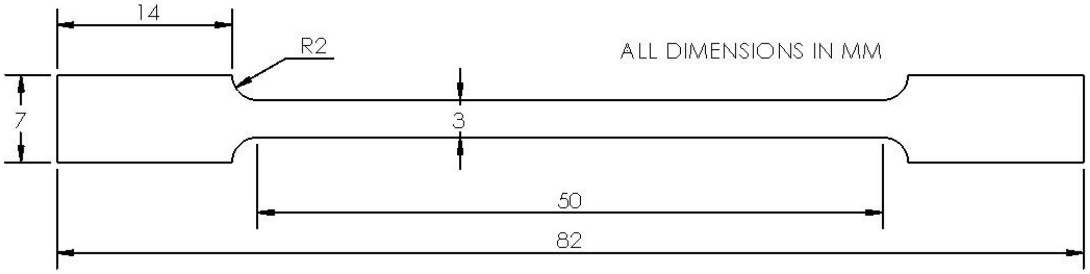

Figure 8: Tensile specimen geometry used in the present study.

The gauge section of the specimen was much longer than what is commonly used. This was done intentionally so that the weld, the heat affected zone (HAZ), and a portion of the base metal would be located within the gage length, far enough from the grip section that the stress could be approximated as a uniaxial tensile stress, in accordance with St. Venant's Principle [25]. This would ensure that the specimen would fail in the location that truly was the weakest link. Before the samples were tested, they were homogenized by heating to 150°C for 5 minutes and rapidly cooling. This was done to thermally cycle the material from martensite to austenite and back, effectively clearing the “thermal memory” of the material by reducing the effect of accumulated dislocations. Room temperature tensile tests were performed on a computer-controlled MTS Insight tensile testing machine at a constant crosshead speed that would result in an initial strain rate of 5×10^{-4} s^{-1} across the reduced length of the tensile specimens. Tensile tests were also conducted at elevated temperatures. The A_f temperature of the material, measured at the center of the weld, was used to determine the temperature at which this tensile test was conducted. It was conducted at 20°C above the A_f temperature, so that the sample would remain as austenite for the entire test. For the high-temperature tensile test, the sample was pulled at a strain rate of 5×10^{-4} s^{-1} until a strain of 2% had been reached. The stress was then reduced to zero, and the sample was again strained, this time to 3% strain. This cycle was repeated for every subsequent 1% strain until the specimen failed.

Microhardness Test

Hardness testing was conducted on the cross-section of the weld at regular intervals in accordance with ASTM E384-17, Standard Test Method for Microindentation Hardness of Materials [26]. Indentations were made in three lines, 0.5 mm, 1.0 mm, and 1.5 mm above the bottom face of the workpieces. A force of 4.9 N (500 mg) was used, and the dwell time was 15 seconds. The first hardness test, conducted on the 450 rpm weld, showed a great deal of scatter in hardness values. Therefore, for the hardness test of the second 400 rpm sample, the sample was first homogenized by heating to 150°C for 5 minutes and cooling.

Optical Microscopy

Optical microscopy was used to view the differences in grain structure within the weld, as well as to check for any weld defects. Areas of interest were viewed in more detail with a scanning electron microscope (SEM) equipped with a backscatter electron (BSE) detector, and energy dispersive X-ray spectroscopy (EDS) was used to find the elemental makeup in these areas. Although the scope of this research was not to optimize the weld parameters to give a defect-free weld, the weld did need to produce a defect-free region large enough for tensile testing. The welds were cut with a water-cooled metallurgical saw with a diamond blade, mounted in epoxy, and then ground on progressively finer sheets of silicon carbide (SiC) metallurgical grinding paper from 120 grit up to 1000 grit. The samples were then polished using 4 µm diamond polishing slurry, and finished with 1 µm diamond polishing slurry. One sample was allowed to naturally age until the grains were visible, while a color tint solution was used to reveal the grains in other samples according to the method described by Bormann et al [27].

For the second 400 rpm weld, a cross-sectional sample was cut and polished before the NiTi backing strip was removed. The polished weld cross sections were viewed under a Zeiss Axiovert 40 MAT microscope, and images were captured with an MRc5 microscope camera. The mean grain size within the stir zone of each weld was measured from the polarized micrographs in accordance with ASTM-E112-10, Standard Test Method for Determining Grain Size. All cross-sectional images displayed follow the convention [28] of putting the advancing side of the weld on the right, and the retreating side on the left.

Theory and Calculation

The ratio of the feed rate and rotational speed used in FSW is referred to as the “pitch,” measured in rotations per millimeter. This parameter can be used to give a very rough comparison of the heat input of different welds. As the pitch is increased, the heat input per unit length of weld decreases, resulting in a “colder” weld. Conversely, as the pitch is decreased, the heat input per unit length increases, resulting in a hotter weld. In addition, welds with a lower pitch generally result in more material mixing, due to the more rapid stirring and higher temperatures seen within the weld [29].

The temperatures at which shape memory alloys undergo a phase transformation are typically described by four numbers. As the cold material is heated, it will transform from martensite to austenite. The temperature at which this transformation begins is called the “austenite start” temperature, denoted “A_s.” The temperature at which the phase transformation is complete is referred to as the “austenite finish” temperature, denoted “A_f”. Since this phase transformation is reversible, the austenite will transform back into martensite when cooled. However, the presence of hysteresis means that the martensitic (cooling) transformation occurs at a lower temperature than the reverse martensitic (heating) transformation. The beginning of the martensitic transformation is marked by the “martensite start” temperature, “M_s,” and the completion of the transformation occurs at the “martensite finish” temperature, “M_f”. These four temperatures can be found from a differential scanning calorimetry (DSC) heating and cooling curve by using the tangent line method, as described in literature [30]. An example of how the tangent line method is applied to a typical NiTi DSC curve can be seen in Figure 9.

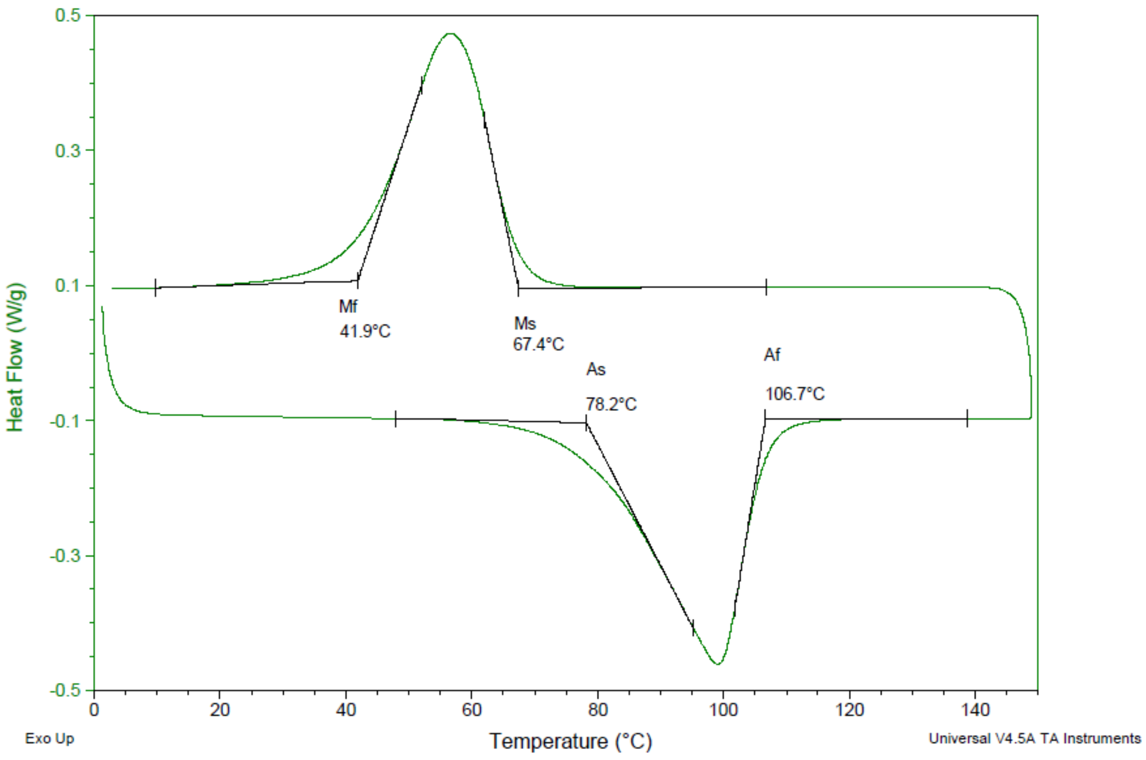

Figure 9: Second cycle DSC curve of the base metal, sample #2. All of the transformation temperatures are marked appropriately.

When testing the strength of a weld, the weld efficiency, or joint efficiency, is used to describe the strength of the weld in comparison to the strengths of the base metals. In dissimilar welds, the maximum possible strength is already limited by the strength of the weaker material, so weld efficiency is the quotient of the UTS of the weld divided by the UTS of the weaker of the base metals, expressed as a percentage. A weld efficiency of 100% indicates that the weld itself is at least as strong as the weaker base metal. Although it is possible for the weld itself to be stronger than the base metal, in such cases the weld efficiency is still expressed as 100%, because in this case the joint strength is limited by the strength of the base metal, and the joint will fail outside of the weld in the base metal. In joints other than simple butt joints, joint efficiency loses its meaning, because the two workpieces may not be of the same thickness, and the force may be transmitted through the joint as a shear force, rather than a tensile force.

One peculiarity specific to dissimilar welds is that the percent strain reported in a stress-strain diagram carries less meaning than it would in the case of a homogenous material. In the case of a dissimilar weld, there are really three distinct zones, the base metal on one side, the weld zone, and the base metal on the other side, all arranged end-to-end in series. The overall elongation measured depends on the length of each of these sections. In the case of a weld where the backing strip is left attached, almost none of the elongation will be observed in the region attached to the backing strip, which also makes the elongation somewhat nebulous.

Results of NiTi to NiTi Welding

Visual Inspection

All welds were visually inspected after completion. In the first 400 rpm weld and the 450 rpm weld, the rear halves of the workpieces were separated approximately 3 mm during the plunge. This was due to inadequate clamping that could not withstand the lateral loads exerted during the plunge phase of the weld. Although the lateral force could have been reduced by reducing the plunge speed, the best solution would simply be to hold the workpieces together more securely. For the 350 rpm weld this was done, and the workpieces did not separate. The separation of the workpieces in the first 400 rpm weld and the 450 rpm weld caused a void to form near the start of the weld, but as the weld progressed, the void went away. This void was clearly not a result of improper processing parameters, so it was disregarded, and only the second halves of these welds were tested. Additionally, all welds stuck to the backing plate. The first set of three welds was pried off of the backing plate with a hammer and chisel. The second 400 rpm weld was placed on a 2 mm thick NiTi backing strip, which was machined off later. To explore the limits of the processing envelope and support the FSW results, FSP was conducted at 300 rpm and 500 rpm. These samples also looked quite satisfactory. It was found that all the combinations of processing parameters tested resulted in welds that contained no defects visible from the surface, as is evident in Figure 10.

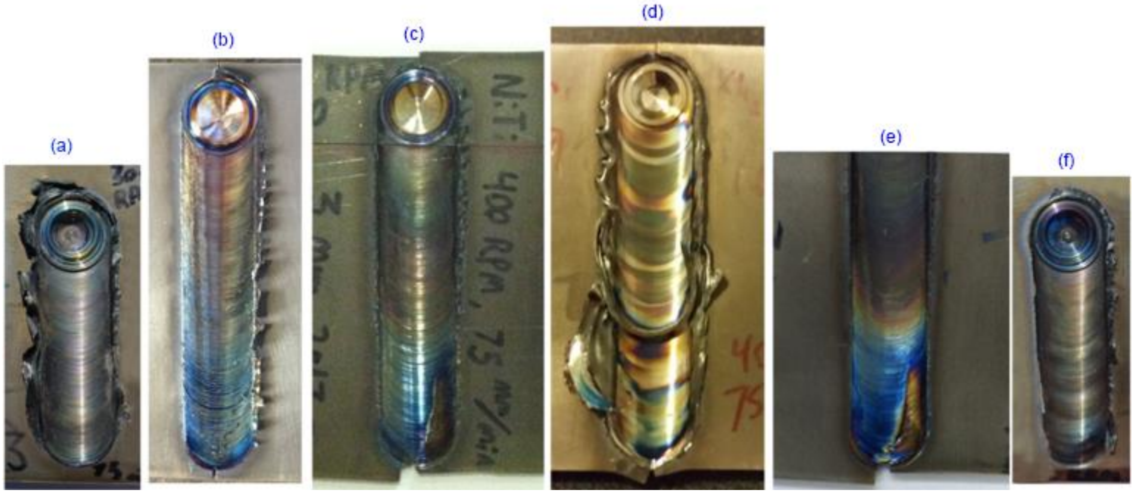

Figure 10: NiTi welds conducted at a constant feed rate of 75 mm/min and at an rpm of: (a) 300 (FSP), (b) 350, (c) 400, (d) 400 – second realization, (e) 450 with withdrawal keyhole removed, and, (f) 500 (FSP).

Optical and Electron Microscopy

The polished cross sections of the first batch of welds can be seen in Figure 11.

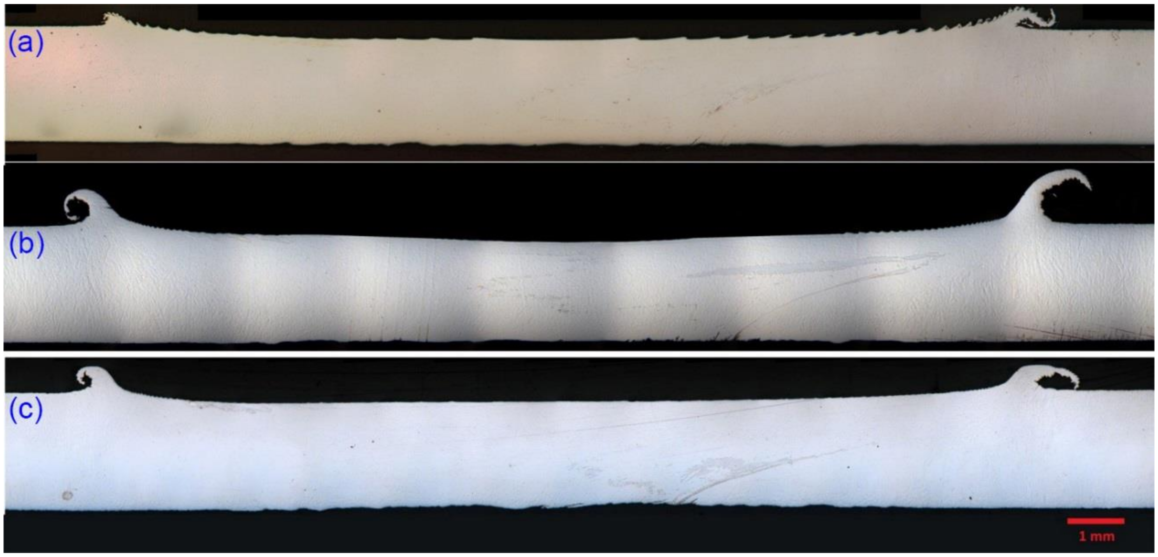

Figure 11: Low-resolution optical microscopy images of weld cross-sections. The welds were conducted at a constant feed rate of 75 mm/min and at an rpm of: (a) 350, (b) 400, and, (c) 450. These images reveal the overall macrostructure of the welds.

It can be seen from these micrographs that there are no large voids or other volumetric defects in any of the welds. There are two relevant features to notice in this image. The first is the horizontal smear in the upper region of the 400 rpm weld on the advancing side. This was investigated in more detail using a scanning electron microscope (SEM), and it was determined that this smear is due to tungsten particles in the weld. It is assumed that rhenium is also present in this location, but the EDS peaks of these two heavy elements overlap significantly. The pattern can be seen in Figure 12, a backscatter SEM image of the tungsten smear. In this image the tungsten, colored white, can be seen to take on the form of ripples.

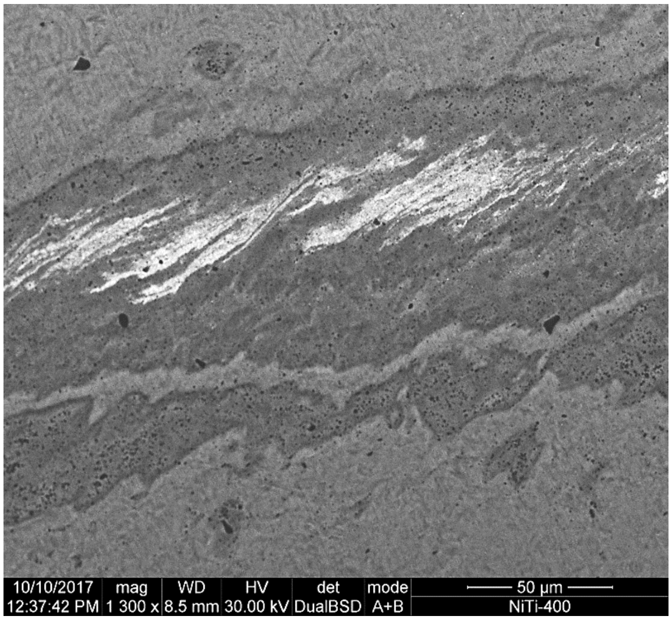

Figure 12: Backscatter electron micrograph of the tungsten smear seen in weld zone conducted at 400 rpm.

A more magnified image was captured to estimate the size of the tungsten-rich particles, and is presented in Figure 13.

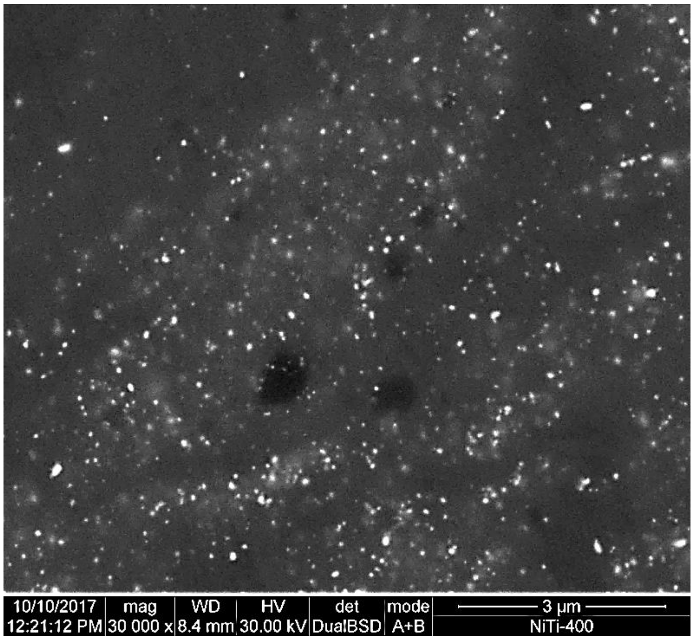

Figure 13: A higher magnification backscatter electron micrograph shows dispersion of nanoscale tungsten-rich particles, likely a result of W-Re tool wear that may have occurred during the welding experiment conducted at 400 rpm.

From this image, it can be seen that the tungsten particles are of very small size, on the order of 75 nanometers. The particles appear to be well-dispersed. Such particles may be suspected of being detrimental to the fatigue strength of the joint; however, this would require further investigation, as it has been reported that Ti_3Ni_4 precipitates smaller than approximately 100 nm do not negatively affect the fatigue strength of NiTi [31]. It makes sense that the tungsten particles are deposited below the shoulder on the advancing side of the weld, because this is where the greatest shear rate and highest temperatures are found.

The second notable feature that can be observed in the cross-section images of the welds is the streak emanating from the bottom of the workpiece on each weld near the advancing side. Energy dispersive X-ray spectroscopy (EDS) was used to find the composition of this streak. It was found to be composed primarily of iron, with small amounts of manganese present. This pinpoints the origin of the streak to the manganese steel backing plate used for the first three welds. So much iron was contained in this streak that pieces of the welded sample could actually be lifted by a strong magnet, as demonstrated in Figure 14. These welds all stuck to the backing plate, and had to be pried off as can be seen in Figure 15.

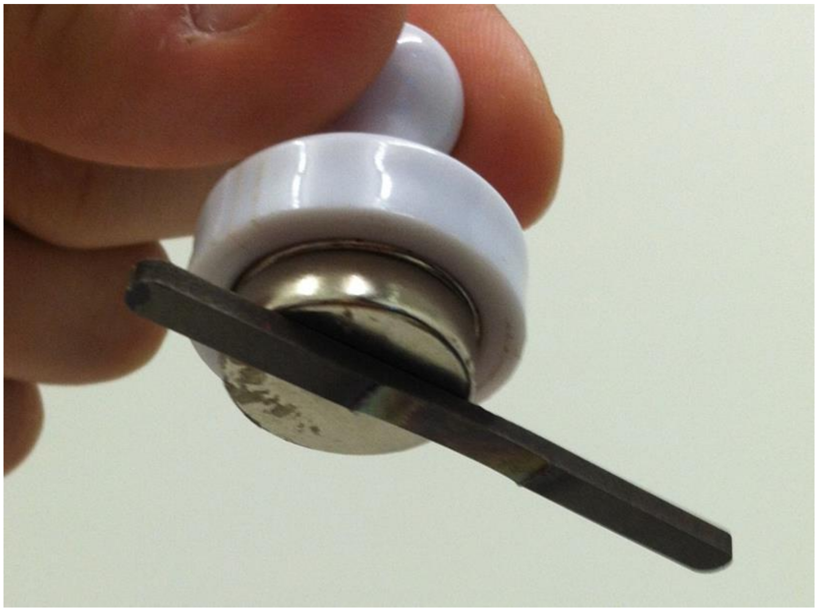

Figure 14: Weld containing the iron streak is attracted by a magnet.

Figure 15: The welded coupons being pried off of the backing plate. In this particular case, welding was carried out at 450 rpm.

It was evident from the surface of the backing plate after the workpiece was removed that the backing plate itself had sustained damage from the welding process. This can be seen in Figure 16.

Figure 16: A typical case of damage to backing plate caused by over-penetration of weld.

This streak of iron weakened the weld considerably, and had to be ground away for useful tensile tests to be conducted. Additionally, the sample welded at 450 rpm was bent slightly in the arduous process of separating it from the backing plate. Because of these reasons, the second 400 rpm weld was performed atop a small backing strip of NiTi. After the weld was completed, the workpieces were stuck to this backing strip, and the entire joint, with the backing strip attached, was cross sectioned for the microscopy that followed. A quick look at Figure 17, a polarized light image of this cross section after being treated with a color tint solution, makes it clear that the stir zone extends approximately 1 mm into the backing plate.

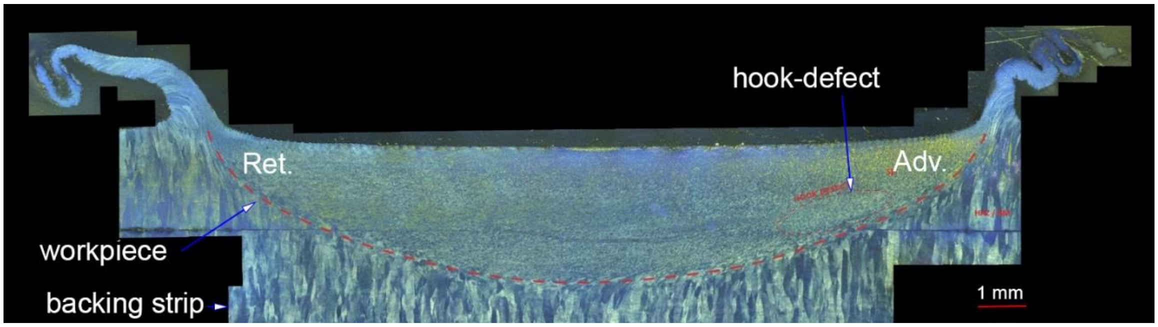

Figure 17: A collage of low-resolution optical microscopy images of the weld cross-section for the second realization of weld conducted at 400 rpm. The sample was treated with color tint solution and viewed under polarized light.

This explains why the workpieces were so difficult to remove from the backing plate, as they were essentially lap welded to it. It should be noted that the tool only had a 1.7 mm long pin, so the pin did not actually contact the backing plate. Although there is no iron-rich streak on the advancing side of this weld, there is a NiTi streak in the same location instead. This streak, better seen in Figure 18, was identified as a “hook defect,” a type of defect that is often seen in friction stir lap welds [32].

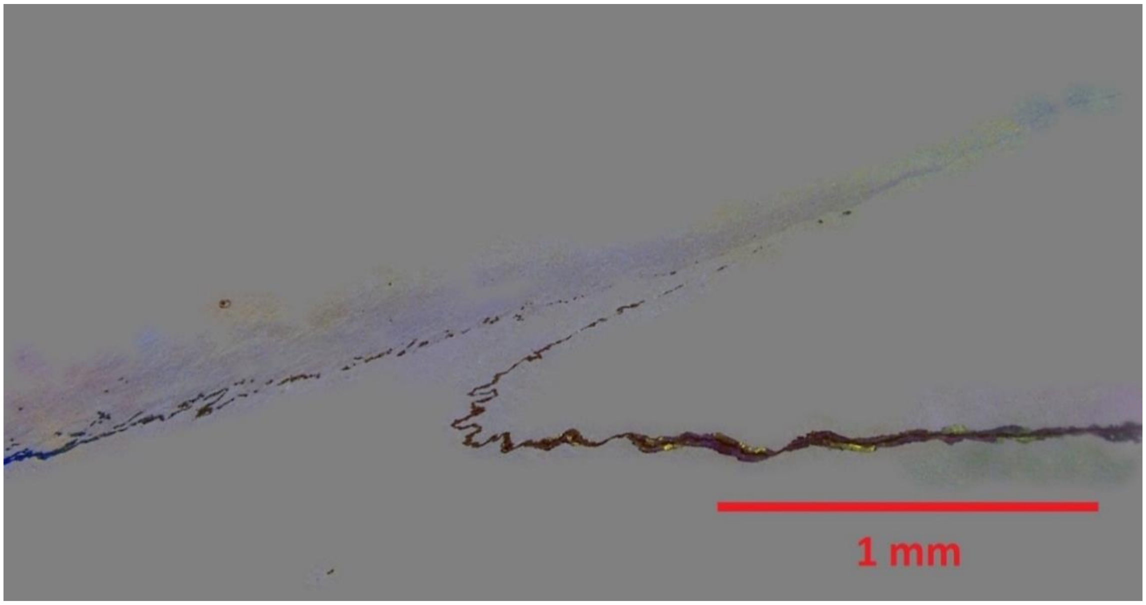

Figure 18: Optical microscopy image reveals the morphology and extent of the hook defect observed in the second realization of the weld conducted at 400 rpm.

By reducing the length of the pin, this hook defect could be avoided. Although not composed of iron, the hook defect in the second 400 rpm weld was still found to weaken the joint. This is because any impurities between the surface of the backing plate and the workpieces were drawn up into the weld at this spot, and since this was at the very edge of the stir zone, the joint was not fully forged here, leaving small voids. Since the scope of this work was not to optimize the welding parameters, but rather to investigate the feasibility of joining NiTi using FSW, the hook defect was excluded from tensile testing by machining away the lower 1 mm of the workpieces in this weld as well.

In contrast to results observed in aluminum alloys [28], a “nugget” was not observed in the cross section of the welded NiTi. There is therefore no distinction between the thermomechanically affected zone (TMAZ) and the stir zone (SZ), so the region of the weld exhibiting grain refinement is henceforth called the stir zone (SZ). The absence of a TMAZ has also been observed in friction stir welds of Ti-6Al-4V [33]. Additionally, in the present study there is no noticeable heat affected zone (HAZ), as the typical microstructural indicators (change in grain size, precipitate growth or dissolution) are not present. Although the HAZ can often be detected from changes in microhardness values, the microhardness profile of the present welds showed no statistically significant changes outside of the SZ that could be attributed to a HAZ. Significant grain refinement was noticeable in the SZ from polarized light microscopy of the cross section of the welds. A detailed view of the grains in the stir zone of the 450 rpm weld can be seen in Figure 19.

The mean grain size in the stir zone of the second 400 rpm weld, measured according to the Heyn Linear Intercept Method, as described in ASTM E112-13 [34] is approximately 20 µm. This stands in contrast to the base metal, which had a mean grain width of roughly 125 µm, and grain length of over 1 mm.

Figure 19: The overall microstructure of the stir zone (SZ), for the weld conducted at 450 rpm. The average grain size in the SZ is 20 µm.

Differential Scanning Calorimetry

Differential Scanning Calorimetry revealed that the welding process caused little change in the transformation temperatures of the material. The DSC results of the base metal can be seen in Figure 20.

This graph is typical of shape memory alloys. The transformation temperatures are highest in the first thermal cycle, and drop a few degrees for the second cycle. After this, the transformation temperatures continue to drop with each successive cycle, albeit less and less. The second cycle DSC results for the center of the second 400 rpm weld are plotted along with the second cycle DSC results for the base metal in Figure 21.

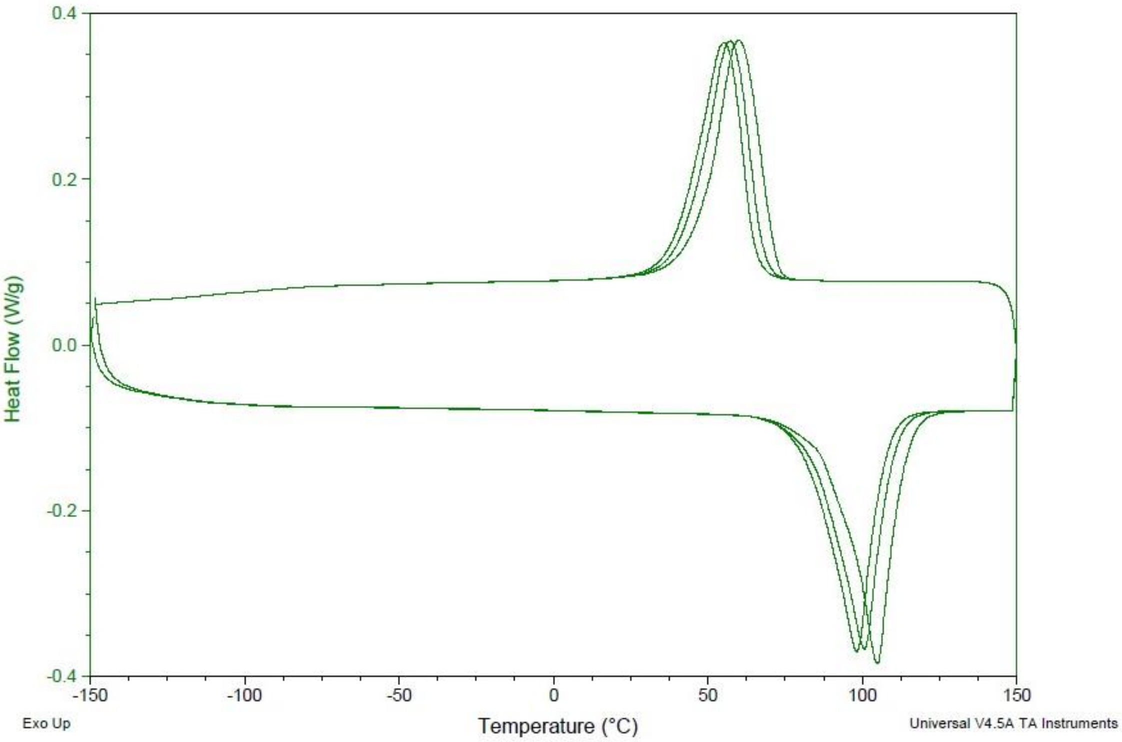

Figure 20: The DSC results for NiTi base metal.

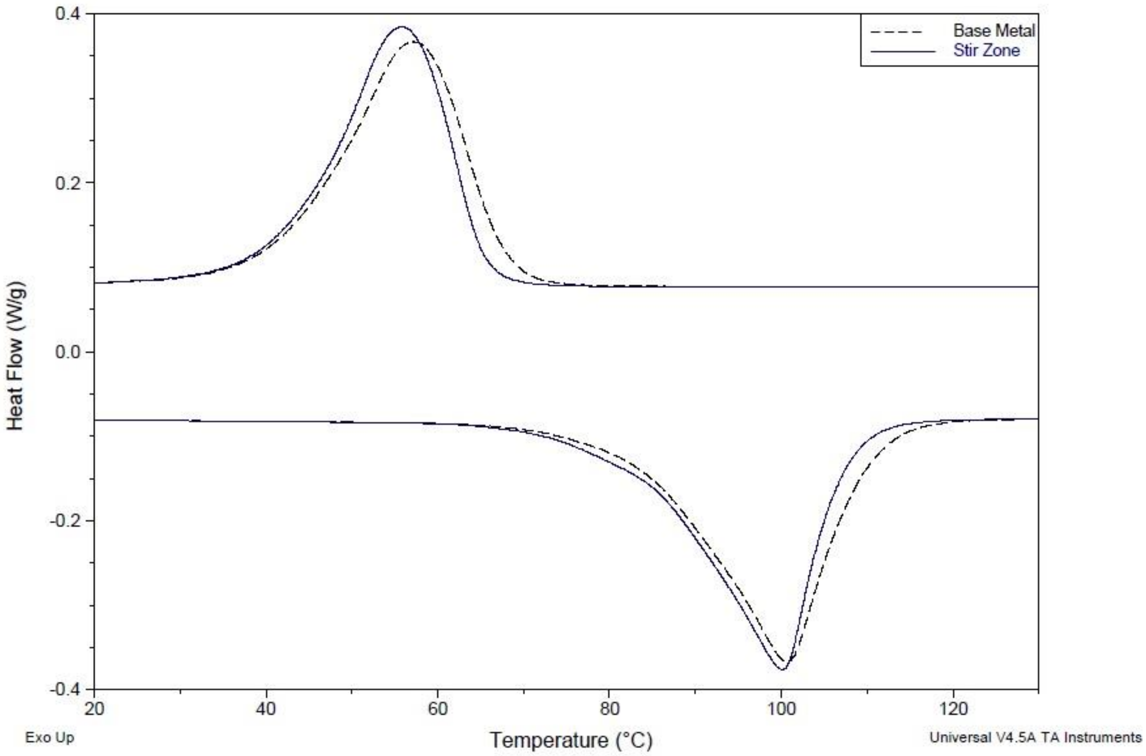

Figure 21: Overlay of cycle 2 DSC results for the base metal and the stir zone of weld conducted at 400 rpm.

From this plot, it is somewhat remarkable to see that there is nearly no difference in transformation temperatures between the base metal and the stir zone. While the base metal had an A_f temperature of 107°C, the center of the stir zone had an A_f of 105°C. A chart of the transformation temperatures measured at intervals along the cross section of the weld can be seen in Figure 22.

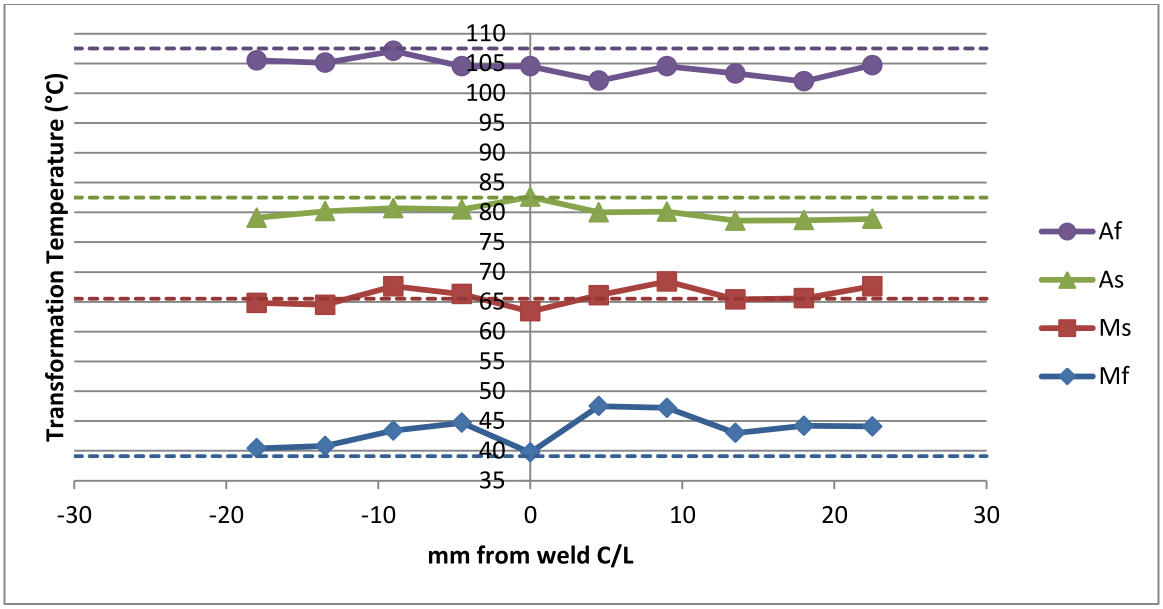

Figure 22: The transformation temperatures taken from DSC results across a welded sample – the dashed lines represent the corresponding values for the base metal.

It should be noted that only the DSC samples at 0, -4, and 4 mm from the weld centerline consisted of material from within the stir zone. The samples at -9 mm and 9 mm may have contained a small amount of material from within the stir zone, but they consisted primarily of coarse-grained NiTi, unrefined by the FSW process.

As a side note, all samples cut from the second 400 rpm weld, except from the sample taken from the very center of the weld, showed an anomaly in their first cycle heating curves in the form of a double-peak. This can be seen in Figure 23, the DSC curve for the sample cut 4 mm from the centerline of the weld on the retreating side.

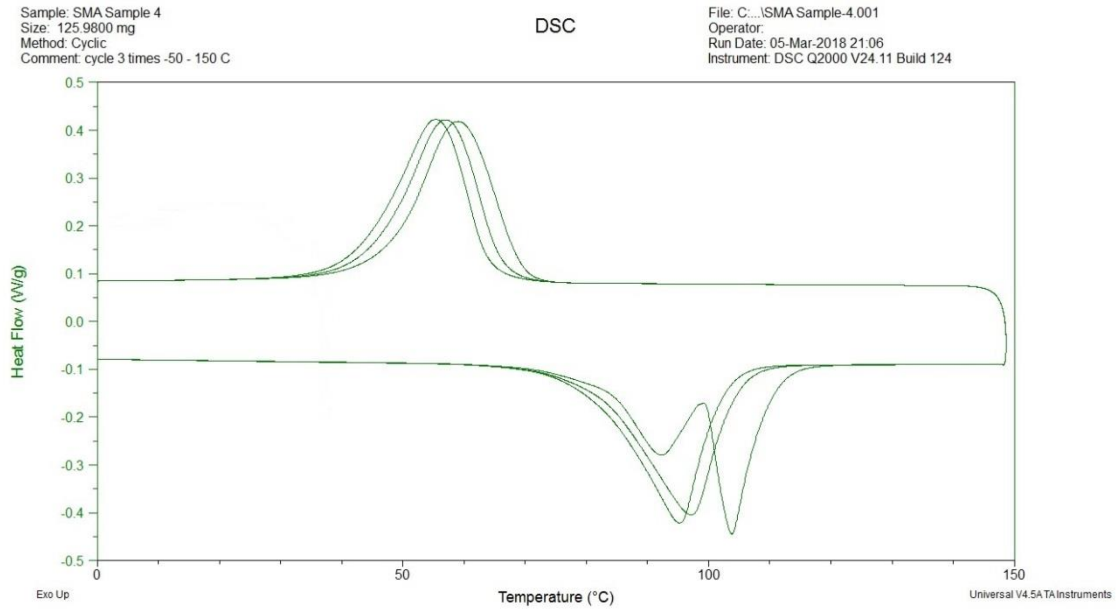

Figure 23: The DSC results for 400 rpm sample, taken at a distance of 4 mm from the weld centerline on the retreating side.

The cause of this double-peak is unclear, as it persisted as far as 22 mm from the weld, far outside the stir zone. A similar double-peak was reported by London et al after FSP of austenitic NiTi [16], but it is unclear whether this double-peak persisted after the first heating cycle. Since the double peak presently observed disappeared after the first cycle, it could be the result of residual stresses from the welding process. Efforts were made to ensure that the double-peak was not merely an artifact of sample preparation, but since it was present in samples cut with a low-speed diamond saw, electric discharge machining (EDM), and EDM with the recast layer removed with abrasive grinding, it was concluded that this double-peak truly does come from the material itself. Some DSC samples taken from other NiTi-NiTi welds did not exhibit this double-peak, indicating that it could be the result of the fixturing conditions during welding. Although it is a mystery of academic interest, it is not a question of practical importance, since it is simple enough to eliminate this double peak with one thermal cycle of the material.

Tensile Response of the Welded Material

The stress-strain diagram of the weld can be seen in Figure 24, where it is plotted alongside the base metal stress-strain data. The base metal was found to have an ultimate tensile strength of 883 MPa, with a failure strain of 40.5%. It is important to note that the first tensile tests of the welded specimens failed prematurely, with one specimen cut from the first 400 rpm weld failing at 268 MPa and 4.9% stress (not shown here for the sake of brevity). This was found to be due to the hook defect on the advancing side of the weld. Therefore, the bottom half of each tensile specimen was removed before subsequent tests. With the hook defect removed, the ultimate tensile strength of the second 400 rpm weld, measured at room temperature, was found to be 818 MPa. The strain at failure was 19.3%, as measured at a 12.7 mm long gage length within the weld zone. The tensile specimen failed in the weld zone, on the advancing side.

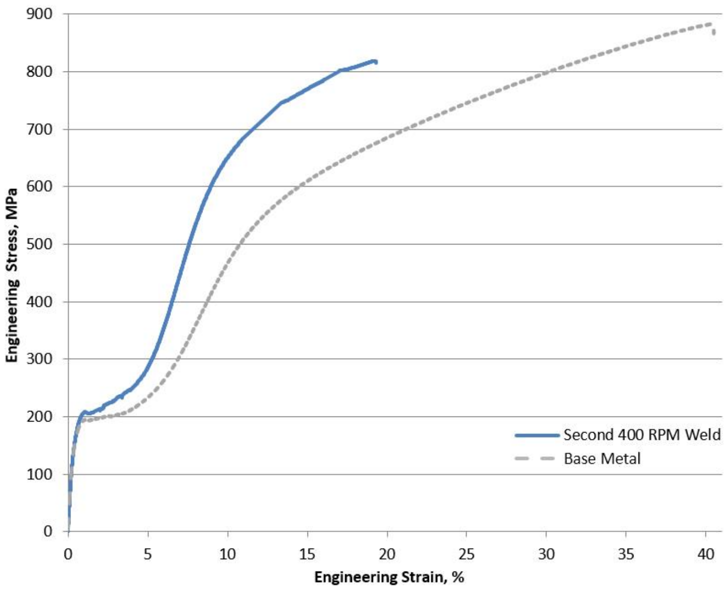

Figure 24: Ambient temperature tensile stress-strain curves of the 400 rpm weld and the base metal.

This results in a weld efficiency of 93%. The weld demonstrates more strain hardening than the base metal, likely due to the smaller grains present in the stir zone of the weld. Although the hook defect was removed from the second 400 rpm welded sample with EDM, it was removed from some of the other samples by mechanical grinding. To ensure that scratches from this process did not act as crack initiation sites, the surface was ground with progressively finer sandpaper, up to 800 grit, leaving the surface with a mirror finish. After the specimen was broken, the surface of the stir zone remained smooth, while the base metal region had a slightly wrinkly texture to it. This was identified as the "orange peel effect," an effect commonly seen in coarse grained materials subject to plastic deformation [35].

The high-temperature tensile test, conducted at 125°C, resulted in an ultimate tensile strength of 540 MPa at a failure strain of 7.7%. This can be seen in Figure 25.

This gives a weld efficiency of 84% when compared to the base metal, which has an ultimate tensile strength of 640 MPa at 37.5% strain, as can be Figure 26.

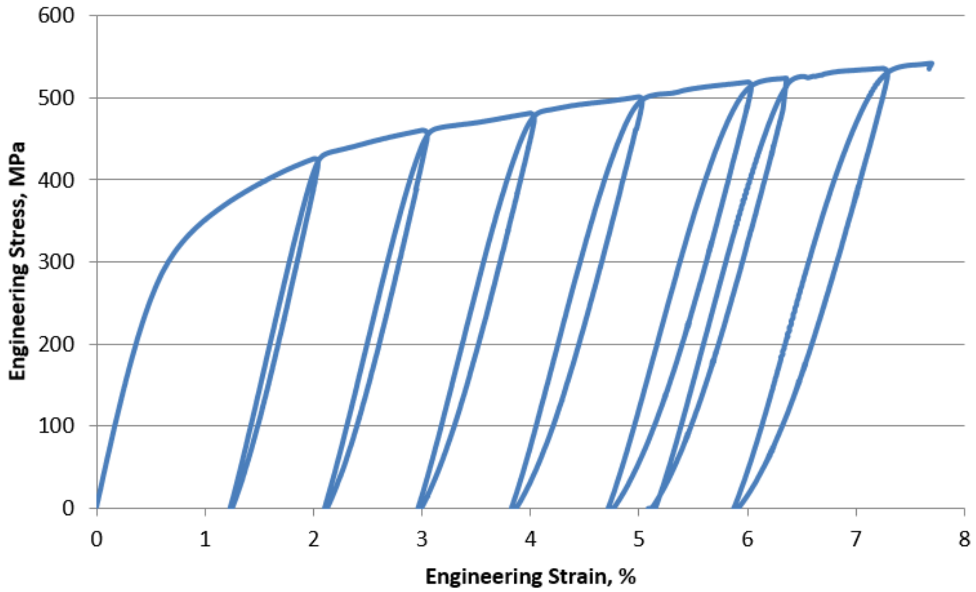

Figure 25: High temperature stress-strain diagram of the final 400 rpm weld.

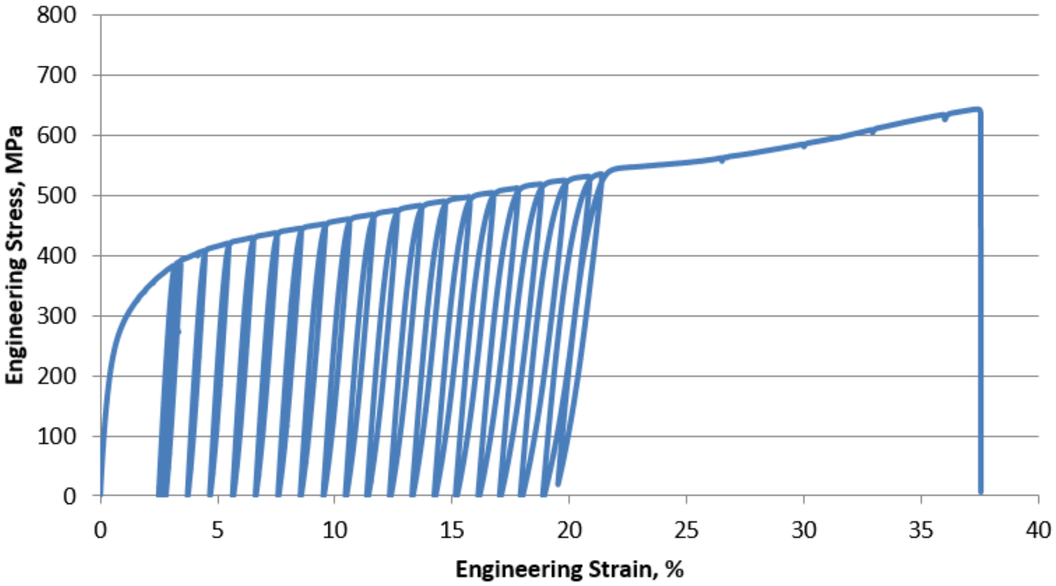

Figure 26: High temperature stress-strain diagram of the base metal.

The high temperature stress-strain diagrams of the weld and the base metal have been overlaid in Figure 27, with the unloading-loading curves removed for clarity.

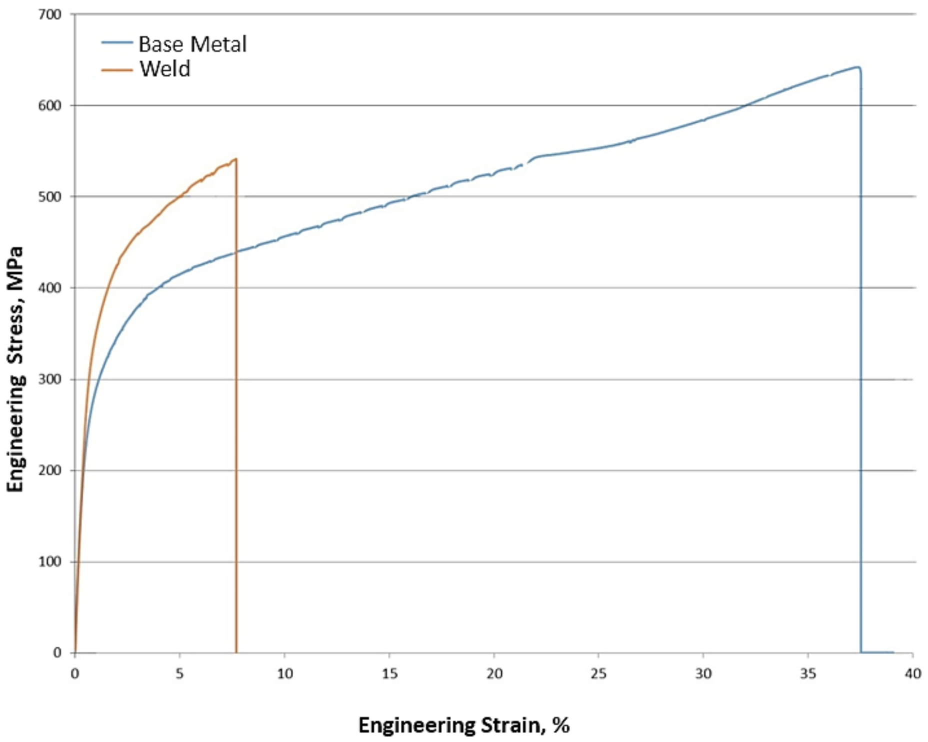

Figure 27: High temperature tensile test - weld vs base metal comparison.

It can be seen from this plot that the weld exhibits more strain hardening than the base metal. This could be predicted by the Hall-Petch relationship [36] due to the much smaller grains seen in the stir zone of the weld.

Microhardness

The set of microhardness data, as measured on the cross section of the 450 rpm weld, had considerable scatter. However, a definite trend of higher hardness near the advancing side of the weld is noticeable. This can be seen in Figure 28, a contour graph of the hardness on the cross section of this weld.

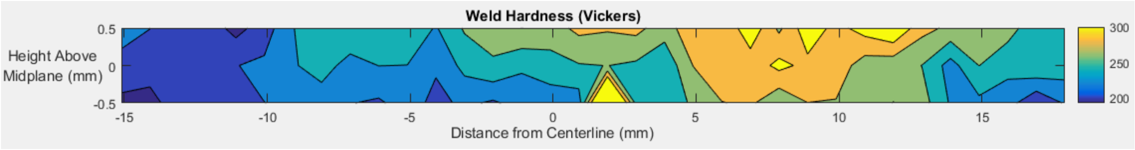

Figure 28: Microhardness contours, 450 rpm weld (right side = advancing side).

The high hardness of roughly 300 HV on the advancing side of the weld, near the top surface, could be a result of the tungsten particles dispersed in the wake of the weld in this area. However, this streak of tungsten did not extend more than 7.5 mm from the weld centerline, while the area exhibiting high hardness extends up to 12 mm from the weld centerline. Therefore, there must be something else at play. The highest hardness value recorded was 395 HV, but this was from an indentation near the iron-rich hook defect. Hardness readings were taken on the cross section along the midplane of the welded sample up to 45 mm from the center of the weld. Even at this distance, there was considerable scatter, as can be seen in Figure 29.

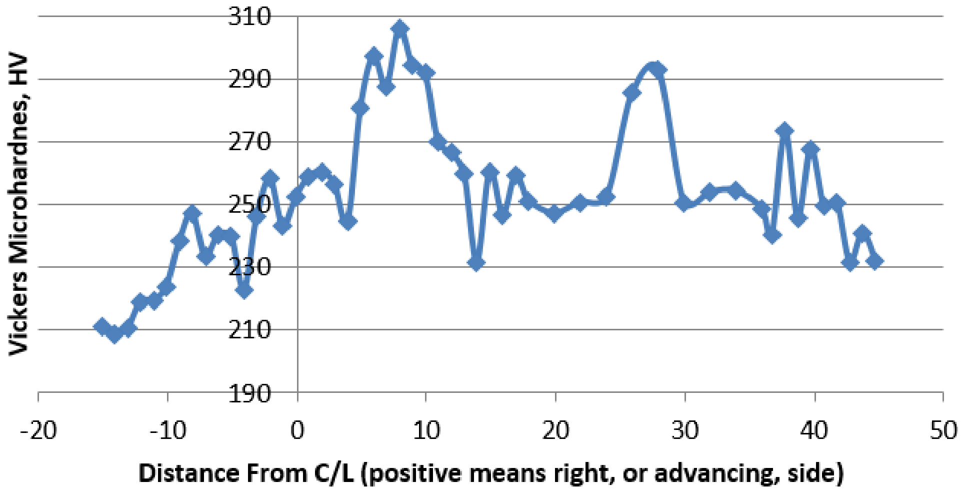

Figure 29: The variations in microhardness of the weld conducted at 450 rpm, taken at a depth of 1 mm.

The first major spike, around +8 mm, was already discussed, while the second major spike, which occurred 27 mm from the weld centerline on the advancing side, may be a result of deformation to the workpieces caused by clamping during the welding process. However, there remains considerable scatter, even apart from these two major spikes.

To check whether this scatter was related to the weld, an extra piece of NiTi was cut and polished, and hardness indentations were performed on it in three rows of 10 indentations, with the same spacing as the indentations on the welded samples. The results of these hardness tests are displayed in Figure 30, using the same Y-scale as the previous plot.

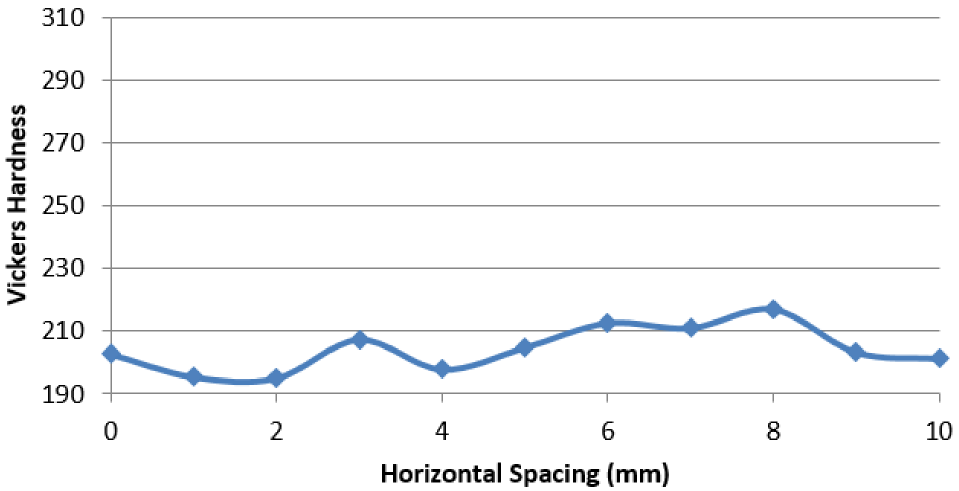

Figure 30: The variations in microhardness of the base metal, taken at a taken at a depth of 1 mm.

It is clear that the base metal itself had far less variation in hardness than the welded sample. The mean value taken from all hardness readings on the base metal is 206 HV, with a standard deviation of 8.5. It should be noted that the average hardness of the 450 rpm welded sample is much higher than this, and even the lowest hardness value recorded on the welded specimen was 208 HV, above the mean of the base metal.

After the second 400 rpm weld was performed, the cross-sectioned sample was heated to 150°C, and then cooled to room temperature. This was done to clear the thermal memory of the sample, in case that was the cause of the scatter in the hardness measurements of the previous sample. This seemed to reduce the scatter somewhat, although outside of the stir zone there was still quite a bit of scatter. Hardness contours of the second 400 rpm welded sample can be seen in Figure 31, which is plotted on the same scale as the 450 rpm hardness contour plot.

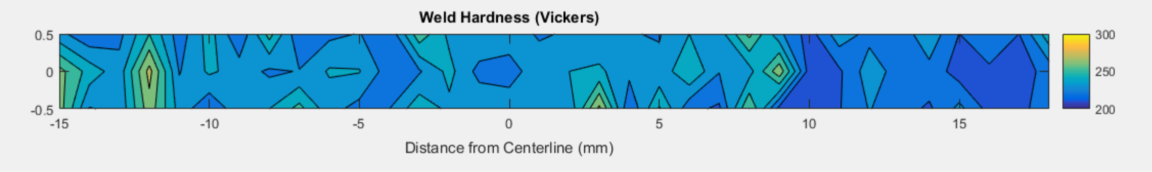

Figure 31: Hardness contours, homogenized 400 rpm weld at same scale as 450 rpm weld.

It is evident that there is less scatter in the 400 rpm homogenized sample than in the 450 rpm sample. For the 400 rpm homogenized sample, indentations were made up to 28 mm on either side of the weld centerline. This full plot can be seen in Figure 32.

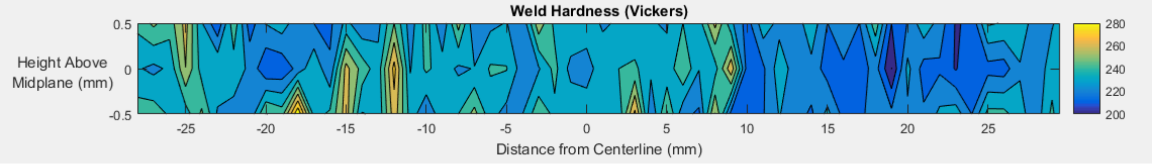

Figure 32: Hardness contours; homogenized 400 rpm weld full cross section.

It should be noted that on this plot in particular, the X and Y axes are on very different scales. This was done for the sake of readability. An image of the second 400 rpm sample, with the indentations visible, is presented in Figure 33.

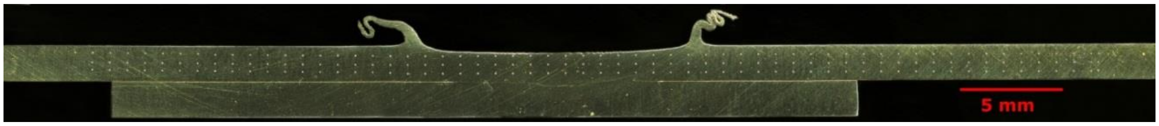

Figure 33: Second 400 rpm weld cross section with indentations visible.

Discussion

The increase in the strain hardening rate seen in the weld is typical of friction stir welded alloys, due to the grain refinement in the stir zone [37]. This, as well as an increase in the yield strength of the material, is beneficial in SMAs, as it can increase the allowable actuation stress and decrease the accumulated irrecoverable strain [38].

Even after the hook defect was identified as a problem on the first set of welds, it was not expected to be a problem on the second 400 rpm weld, since the backing plate and the workpieces were composed of the same material. However, after the high temperature tensile test of this weld was conducted, it was found that it fractured in the location of the hook defect. The location of fracture is marked in red in Figure 34, while the green horizontal lines indicate the top and bottom faces of the tensile specimen. The blue line marks the interface between the workpieces and the backing strip, and it can be seen that this interface rises on the advancing side of the weld, forming the hook defect, at the location of fracture. The hook defect was machined away before the room temperature tensile test of this weld was conducted. It is likely that if the hook defect had been machined away for the high temperature tensile specimen, it would have failed at a higher stress.

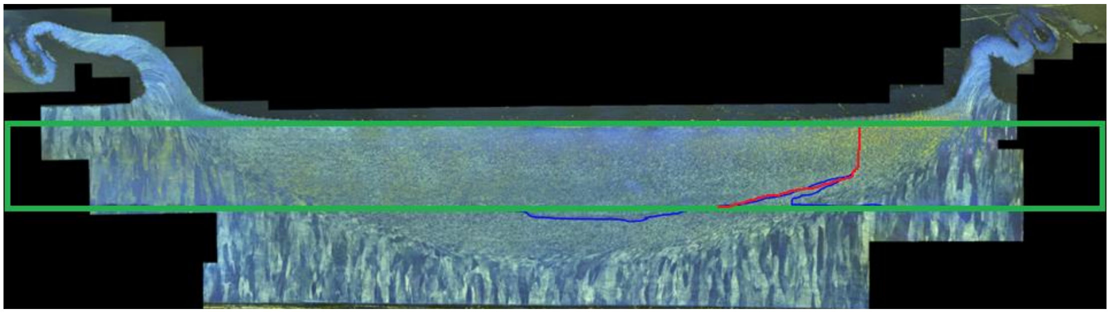

Figure 34: Cross-section of second 400 rpm weld, fracture surface of high temperature tensile test marked in red.

The amount of scatter seen in the hardness profiles is somewhat surprising. This scatter may be a result of the large thermal stresses experienced in the base metal, in conjunction with the coarse grain structure. Studies on the residual stresses resulting from FSW of Ti-6Al-4V indicate that large compressive residual stresses near the top of the workpiece extend out far on either side of the weld [33]. If this were the case in the present study, it is likely that a grain of martensite could reorient to accommodate these residual stresses, depending on the crystallographic orientation of the grain to begin with. Since the grains in the stir zone are so coarse, most microindentations would only be striking one or two grains. Because of this, the orientation of the grains will have a much larger effect on the individual hardness readings than they would if the grains were much smaller than the indentations.

Based on the DSC results, the welding process caused very little change in the transformation temperatures of the material. This is somewhat surprising considering the large change in transformation temperatures that is caused by other severe plastic deformation processes such as equal channel angular extrusion (ECAE) [39]. In fact, a second DSC button was cut from the base metal, and it was found that the transformation temperatures between the two base metal samples differed by 4°C. In light of this variation in the base metal transformation temperatures, it is quite possible that the variation seen in the transformation temperatures of the welded specimen was present even before the welding took place. When comparing the effects of FSW and ECAE on the transformation temperatures of the SMA, it must be kept in mind that the temperatures reached in FSW of NiTi are much higher than the temperatures at which ECAE was performed. Although the exact temperatures within the stir zone were not measured, they can be estimated by the visible thermal radiation emitted by the tool and the region of the workpiece immediately surrounding it, as seen in Figure 35.

Figure 35: Glowing orange tool during welding of 350 rpm sample.

During the welding of the 350 rpm samples, the tool and surrounding flash were specifically noted to be glowing red-orange during the welding of the 350 rpm sample, corresponding to a temperature of roughly 900°C [40]. This agrees with the published literature reporting that peak temperatures in FSW tend to be approximately 80% of the absolute melting point of the metal [13]. This is much higher than the 300°C processing temperature at which ECAE was performed, so it is really not surprising that the results of the two processes on the transformation temperatures were much different.

Summary

The following are the conclusions based on the above results:

- Friction stir welding can be used to successfully weld NiTi SMAs. The processing envelope for FSW of NiTi at a feed rate of 75 mm/min ranges from spindle speeds of 300 to 500 rpm, and likely beyond. The weld efficiency was found to be 93% at room temperature and 84% at elevated temperatures.

- Friction stir welding of martensitic NiTi results in considerable grain refinement of in the stir zone of the weld but causes rather minor (no more than 7°C) changes in the transformation temperatures of the material.

- Under tensile loads, the fine grained stir zone causes more strain hardening in the welded material than the base metal. Significant scatter exists in the microhardness measured on the cross-section of the weld, indicating that residual stresses may be present in the material.

- The W-Re tool experiences some wear, as tungsten particles, approximately 75 nm in size, were deposited below the shoulder of the weld on the advancing side for the 400 rpm weld.

CHAPTER III

DISSIMILAR FRICTION STIR WELDING OF NiTi

After NiTi-NiTi welds had been successfully performed at a broad range of welding parameters and characterized, the focus was shifted to FSW of NiTi to dissimilar metals.

Dissimilar FSW Experimental

Dissimilar welds to NiTi were performed using the same base metal source that was used in the similar NiTi-NiTi welds. However, the slabs were not cut in half as they were for the previous tests. Rather, they were left whole, and welds were performed on all four edges of the slabs. Once again, the slabs were lightly sanded prior to welding to remove the EDM recast layer.

Welding Process

Before dissimilar welds were attempted, similar welds were performed on each of the candidate materials to determine welding parameters for each material. In order to narrow the parameter space, the initial set of parameters was based on successful parameters reported in published literature, as summarized in Table 4. These parameters, along with knowledge of the thermomechanical properties of each material, guided the selection of the processing parameters for the dissimilar welds.

Table 4: A summary of FSW parameters reported in literature for similar welds of Ti-6Al-4V, Inconel 625, and 304 stainless steel.

Workpiece Material	Tool Material and Geometry	FSW Parameters	Outcomes
Ti-6Al-4V 2 mm thick	W-Re Ø11 mm shoulder 1.8 mm long conical pin, tapering from 6 to 4 mm diameter	400-600 rpm 75 mm/min 2.5° tilt angle	Weld UTS: 915-975 MPa. Higher rpm resulted in more ductility, at the expense of strength [22]
Inconel 625 2 mm thick	WC-Co Ø15 mm shoulder 1.8 mm long pin Ø6 mm pin	200 rpm 100 mm/min 3° tilt angle	Weld UTS: 900 MPa Some tungsten found in weld Bottom of workpieces reached 800 °C [41]
304 Stainless Steel 2.5 mm thick	W-Re Ø13 mm shoulder 2.4 mm long pin Ø6 mm pin	600 rpm 120 mm/min	Defect-free (not tensile tested)[42]

The same W-Re tool that was used in the previous section was used in this section, at a 2.5° tool tilt angle unless otherwise specified. Once again, all welds depicted, and cross-sections thereof, follow the convention of displaying the advancing side of the weld on the right and the retreating side on the left [28].

Published literature on the welding parameters of Ti-6Al-4V indicates that when a tool with an 11 mm diameter shoulder is used, the processing envelope ranges from 400 rpm to 600 rpm at 75 mm/min [22]. Since the tool presently used had a larger shoulder, it could be expected that the same amount of heat could be produced with a lower rotational speed, so a spindle speed of 400 rpm was used. Initial trials of FSW Ti-6Al-4V produced extremely poor welds, as can be seen in Figure 36, an image of a weld performed at 400 rpm and 75 mm/min without shielding gas. However, Ti-6Al-4V friction stir welds improved when argon shielding gas was employed, and argon was used for the rest of the welds, including dissimilar welds with NiTi.

Figure 36: Preliminary Ti-6Al-4V weld performed without shielding gas.

It has been reported that Inconel 625 can be successfully friction stir welded at 200 rpm and 100 mm/min [41]. However, 100 mm/min seemed like quite a high feed rate, so to reduce the risk of damaging the tool, a feed rate of 75 mm/min was used instead. The 30kN friction stir welding machine was unable to provide enough torque to keep the tool turning at 200 rpm, so halfway through the weld the feed rate was reduced to 35 mm/min to produce more heat in the weld zone and reduce the required torque. This weld can be seen in Figure 37.

Figure 37: Preliminary Inconel 625 weld performed at 200 rpm and 75 mm/min (reduced to 35 mm/min).

Finally, two pieces of 304 stainless steel were welded together at 400 rpm and 75 mm/min. These parameters were obtained by scaling the rotational speed and feed rate reported by Plaine and Alcantara [42] to result in a feed rate of 75 mm/min while keeping the pitch relatively constant. These scaled parameters resulted in a good weld that can be seen in Figure 38.

Figure 38: Preliminary 304 stainless steel weld, performed at 400 rpm and 75 mm/min.

The welding parameters used in each preliminary similar weld are summarized in Table 5.

Table 5: Welding parameters used for preliminary similar friction stir welds.

Material	Rotational Speed	Feed Rate
NiTi	400 rpm	75 mm/min
Ti-6Al-4V	400 rpm	75 mm/min
Inconel 625	200 rpm	35 mm/min
304 Stainless Steel	400 rpm	75 mm/min

The welding parameters listed in Table 5 influenced the selection of welding parameters for the first dissimilar weld of each combination of materials. The parameters subsequently used for dissimilar welds are listed in Table 6. It should be stressed that the parameters were not predetermined for all fourteen welds. Rather, the results of previous welds were used to guide the selection of parameters for subsequent welds.

Table 6: The friction stir welding test matrix used for dissimilar welds.

Weld	Dissimilar Metal	Rotational Speed (rpm)	Feed Rate (mm/min)	NiTi on [RS/AS?]	Notes	Selected for detailed analysis?
1	Inconel 625	350	75	Retreating Side	Not depicted	-
2	Inconel 625	250	50	Retreating Side		-
3	Inconel 625	250	35	Retreating Side	Tool offset 1.5 mm to NiTi side. Shoulder mushrooming	-
4	Ti-6Al-4V	400	75	Retreating Side	Overloaded machine, surging feed	Yes
5	Ti-6Al-4V	400	75	Retreating Side	Re-machined tool	-
6	Ti-6Al-4V	500	50	Advancing Side	Niobium Interlayer was used	Yes
7	Ti-6Al-4V	200	35	Advancing Side		-
8	Ti-6Al-4V	400	50	Retreating Side	Niobium backing strip	-
9	304 Stainless	400	75	Retreating Side		Yes
10	304 Stainless	750	75	Advancing Side		-
11	304 Stainless	500	75	Advancing Side		-
12	304 Stainless	500	40	Advancing Side		Yes
13	304 Stainless	500	50	Advancing Side	1.5° tilt	-
14	304 Stainless	500	60	Advancing Side	1.5° tilt	-

The NiTi-Inconel 625 welds, with the exception of Weld 1, are depicted in Figure 39. All three NiTi-Inconel welds were of poor quality. The NiTi-Inconel welds resulted in extensive tool wear, seen in Figure 40, and the shoulder was almost completely cone-shaped. Due to the poor nature of these first three dissimilar welds, the focus was shifted to welding NiTi to Ti-6Al-4V.

Figure 39: NiTi-Inconel 625 Weld 2 (left) and Weld 3 (right).

Figure 40: Tool After NiTi-Inconel welds. Deformation of the shoulder is visible.

The results of all attempts at welding NiTi to Ti-6Al-4V can be seen in Figure 41. It is quite evident that none of the parameters tried resulted in quality welds. Weld 4 was cross-sectioned for further investigation. All welds between Ti-6Al-4V and NiTi left deep channels in the wake of the pin, but Weld 6, which exhibited a very smooth channel, was cross-sectioned and polished to investigate the effects of the 0.2 mm thick niobium interlayer used in this weld. Overall, the results of the dissimilar welds made between NiTi and Ti-6Al-4V were not much better than those made between NiTi and Inconel 625, so the focus was shifted to dissimilar welding with 304 stainless steel.

Figure 41: All NiTi to Ti-6Al-4V welds (Welds 4-8), from left to right.

Initially, only one dissimilar weld was made between NiTi and 304 stainless steel. This weld, labeled Weld 9, is depicted in Figure 42. While there is a channel that runs the entire length of the weld, it only extends about 1 mm deep, halfway into the workpieces. Below that, the two materials actually were joined. Additionally, due to an overly long tool pin, both workpieces were found to be fused to the backing strip, which was another 2 mm thick piece of 304 stainless steel. Although it was clearly not a desirable weld, Weld 9 was better than any of the dissimilar welds with Inconel 625 or Ti-6Al-4V, and was used for further testing. A cross-section of the weld was cut and polished for microscopy and microindentation, and after the channel defect was eliminated by machining away the top millimeter of the workpieces, the remaining portion of the weld was cut into tensile specimens and differential scanning calorimetry samples.

Figure 42: Weld 9, NiTi to 304 stainless, performed at 400 rpm and 75 mm/min.

After characterization of Weld 9 was complete, additional welds with stainless steel were carried out. Various sets of parameters were tried for these last welds, labeled as Welds 10-14 and depicted in Figure 43, but upon visual inspection, none of them produced a defect-free weld. However, defect-free regions can be seen in Welds 12 and 14. Therefore, Weld 12 was cross-sectioned and polished as well, so that a defect-free cross-section of a NiTi-stainless steel friction stir weld could be further investigated.

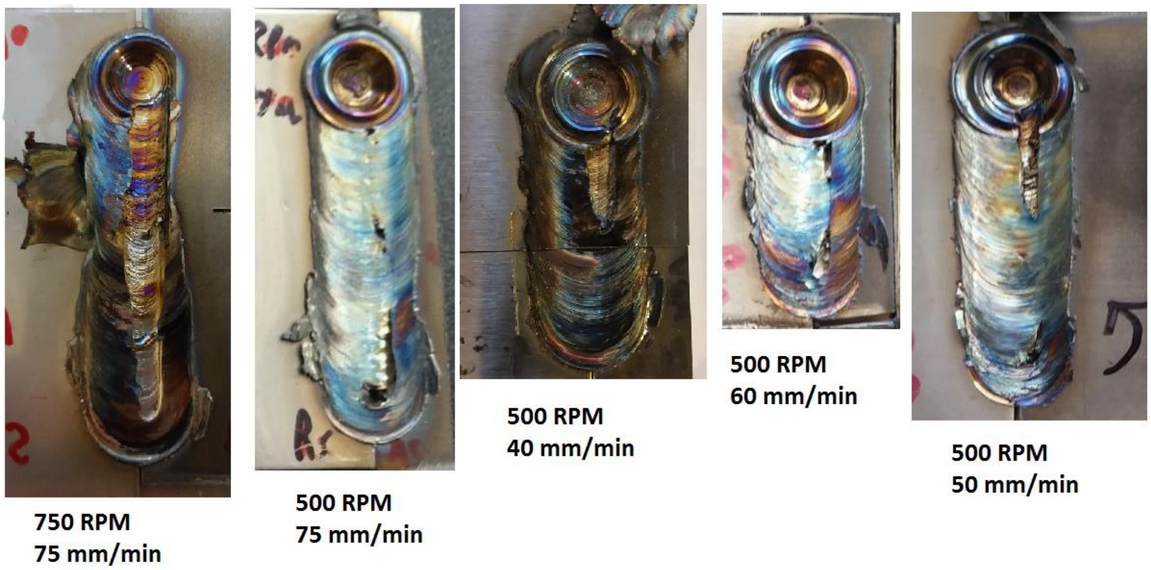

750 RPM
75 mm/min

500 RPM
75 mm/min

500 RPM
40 mm/min

500 RPM
60 mm/min

500 RPM
50 mm/min

Figure 43: NiTi to 304 stainless, from left to right: Weld 10, 11, 12, 13, and 14.

Optical and Electron Microscopy

Microscopy was essential for understanding the effects of the FSW process on material mixing, grain refinement, and welding defects. First, welded specimens were cut with a slow-speed metallurgical saw with a diamond blade to expose their cross-sections.

These samples were then mounted in epoxy and the surface was made planar by grinding with silicon carbide (SiC) grinding pads starting from 120 grit and culminating in 1000 grit. To obtain a mirror-surface on the samples, they were then polished with 4µm diamond polishing slurry, and finished with 1 µm diamond slurry. These samples were then photographed under an optical microscope, and the photos were stitched together to obtain macro-scale high resolution images of the full cross-sections.

Next, the welds were tint etched by immersing in a solution of 120 mL of distilled water, 15 mL of concentrated 12M (37 wt.%) HCl, 15 g of $Na_2S_2O_5$ powder, 10 g of $K_2S_2O_5$ powder, and 2 g of NH_4FHF crystals for 60 seconds, as detailed by Bormann et al [27]. Although this method was effective at revealing the grains of similar NiTi welds when viewed under polarized light, it was found that when a dissimilar weld was immersed in the solution, it preferentially darkened only one metal, and did not color the grains. This may be due to the dissimilar metals acting as a galvanic corrosion cell, and the less noble alloy being selectively attacked by the solution. Although this made it difficult to view the grain structure on either side of the weld, it did differentiate the two metals with great contrast, which made it much easier to see the degree of mixing that occurred. It was decided that due to the different chemical properties of the two metals, the two sides of the weld would need to be etched independently. The NiTi grains were observed by first masking off the stainless steel side of the weld, and then etching the exposed NiTi side using the same tint etch solution that was used earlier. This allowed the NiTi grain structure to be seen under polarized light. The average grain size within the stir zone on the NiTi side was then measured using the Heyn Lineal Intercept Method, as detailed in ASTM E-112 [34].

To investigate the mixing between NiTi and stainless steel in more detail, the Weld 9 sample was repolished and viewed under a scanning electron microscope (SEM). A backscatter electron (BSE) detector was fitted to the microscope so that the image could be contrasted by atomic number. This did not provide as much contrast as the tint etch solution, but it allowed the interface between the NiTi and stainless steel to be viewed in more detail. Energy dispersive X-ray spectroscopy (EDS) was used to generate an elemental map of the weld, which agreed with the results of the tint etch contrast method. Finally, an EDS linescan was performed across the NiTi-stainless steel interface in order to determine how much diffusion occurred between the two materials. All cross-sectional images displayed follow the convention of putting the advancing side of the weld on the right, and the retreating side on the left.

Differential Scanning Calorimetry

After the stainless steel backing strip was removed from the NiTi to stainless steel weld, labeled Weld 9, differential scanning calorimetry (DSC) samples, 3 mm in diameter and 1 mm tall, were cut from the weld as seen in Figure 44. DSC is a useful method of measuring the transformation temperatures of a shape memory alloy sample. Since the stainless steel was not expected to undergo any phase transformations in the temperature range tested, only one DSC sample was cut from the stainless steel side. Most of the DSC samples were tested by cooling to -50°C, then heating to 150°C and cooling back down to -50°C for three cycles at a rate of 10°C/min. However, the first sample tested, the DSC sample from the center of the weld where the two metals meet, was cycled between -150°C and 150°C for three cycles. This was done because it is known that when small amounts of iron are added to NiTi, as would be expected in the diffusion zone of the joint, the transformation temperatures can be depressed to as low as -140°C [43]. After DSC was conducted on the sample cut from the region containing the NiTi-stainless steel interface and it was seen that no transformations occurred below 0°C, the rest of the samples were only cycled as low as -50°C. Two DSC samples were also cut from the base metal. The results from these two samples not only served as a control to compare the welded samples to, but also gave an idea as to the amount of random scatter to be expected in DSC curves due to either inhomogeneity of the base metal or precision error in the DSC machine.

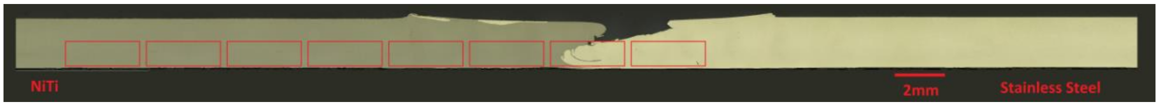

Figure 44: Location of DSC samples cut from Weld 9.

Tensile Response of the Welded Material

After the top 1 mm of material was removed from Weld 9 by EDM, tensile specimens were cut transverse to the welding direction, according to the same geometry as in the previous section.

For the first Weld 9 tensile specimen, the stainless steel backing strip was left attached. However, for subsequent tensile specimens, the backing strip was removed by EDM. The tensile specimen with the backing strip attached, seen in Figure 45, was tensile tested at room temperature using a laser extensometer. The sample was tested in a computer controlled MTS Insight tensile testing machine at a constant crosshead speed that was calculated to result in an overall strain rate of $5x10^{-4}$ s^{-1} in the reduced area.

Figure 45: Weld 9 (NiTi-stainless) tensile specimen with backing strip attached.

Tensile specimens with the backing strips removed were also tested at room temperature at the same strain rate. For these tests, an MTS LX1500 laser extensometer was used to measure the strain. Although this extensometer provides a lower strain resolution than a conventional contact-type extensometer, it has the advantage of not applying a lateral force to the long and slender tensile specimen. Additionally, the laser extensometer was capable of measuring the strain in three different segments of the specimen simultaneously. This proved useful for the testing of the inhomogeneous tensile specimens cut from the dissimilar NiTi-stainless steel weld, since the variation in the mechanical properties could be captured by strain measurements in three different areas.

Finally, a tensile specimen with the backing strip removed was tested at 121°C, which was 20°C above the A_f temperature measured in the weld. This high temperature tensile test was conducted in an LBO-series Thermocraft LabTemp environment chamber with a thermocouple attached to the center of the tensile specimen to monitor its temperature. This specimen was tested at the same crosshead speed as the other specimens.

Microhardness

Hardness tests, spaced every one millimeter, were conducted on the polished cross section of Weld 9 in accordance with ASTM E384-17, Standard Test Method for Microindentation Hardness of Materials [26]. A force of 4.9 N (500 mg) was used, and the dwell time was 15 seconds.

Results

Optical and Electron Microscopy

Cross-sections cut from Welds 4, 6, 9, and 12 were analyzed by optical microscopy, and Weld 9 was then analyzed by electron microscopy. The cross-section of Weld 4, NiTi to Ti-6Al-4V, can be seen in Figure 46. There is a very large amount of flash present on the NiTi (retreating) side, most likely because the worn tool shoulder was unable to properly contain the plasticized material. It appears that, at least in the location of this cross-section, the Ti-6Al-4V was drawn down under the pin into the root of the weld, and NiTi was expelled as flash. It is also apparent that there is not very much mixing of the two materials. Rather, a fairly linear interface is observed on the retreating side of the weld. The center of the weld was thinned by the welding process so that only about 0.88 mm of material was left. It is likely that the cross-section of the weld varies significantly along its length, due to the erratic motion of the tool that resulted from excessive downforce. This variation in cross-section, combined with the unrepeatable nature of the weld, precluded tensile testing of this weld.

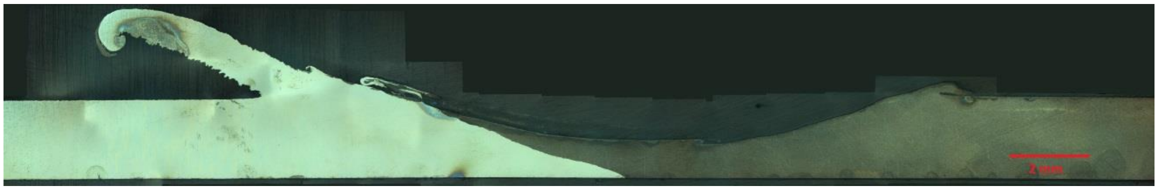

Figure 46: A collage of low-magnification optical microscopy images of the cross-section of Weld 4, NiTi to Ti-6Al-4V. The sample was treated with a tint etch solution and viewed under polarized light.

The NiTi to Ti-6Al-4V weld with the niobium interlayer, Weld 6, was cross-sectioned and polished, and the cross-section is presented in Figure 47. It can be seen that the remaining portion of the workpiece under the gouge is only about 0.3 mm thick. The stir zone of this weld is depicted in Figure 48, with the remains of the niobium interlayer visible. It appears that in this weld, all of the material that was in the tool’s path was deposited as flash on the advancing side of the weld. This is atypical, as usually the retreating side of the weld has more flash. Once again, this thin amount of material remaining in the joint was deemed unsuitable for mechanical testing.

Figure 47: A collage of low-magnification optical microscopy images of the polished cross-section of Weld 6. NiTi is on the advancing (right) side of the weld, while Ti-6Al-4V is on the retreating side.

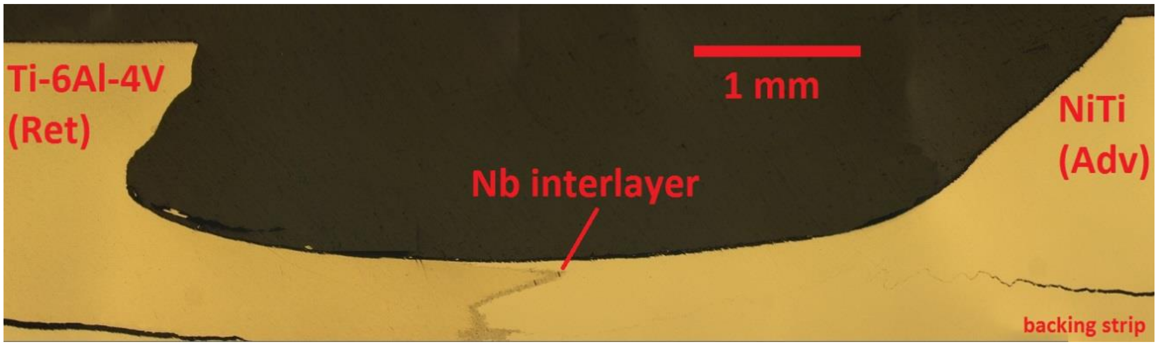

Figure 48: A detailed view of the stir zone of Weld 6, NiTi to Ti-6Al-4V with a niobium interlayer.

The cross-section of Weld 9, the first NiTi-stainless steel weld performed, is shown in Figure 49. It is evident that the channel is offset to the advancing (stainless steel) side of the weld. Although a small gap can be seen circled between the workpieces and the backing strip near the edges, there is no gap visible directly under the weld itself because the tip of the tool pin came very close to the backing strip, lap welding it to the workpieces. Additionally, a small void can be seen circled in Figure 50 at the interface between the two metals below the channel. There is very little flash present, indicating a relatively low downforce. By increasing the plunge depth slightly, the downforce would have increased, which may have closed up this void.

Figure 49: A collage of low-magnification optical microscopy images of the cross-section of Weld 9, with the stainless steel backing strip attached. A small gap between the backing strip and the workpieces is circled.

Figure 50: Detailed view of Weld 9 (NiTi-stainless) stir zone, with void circled in red.

A polarized light image of the same weld after being immersed in the tint etch solution for 60 seconds can be seen in Figure 51. The tint etch solution provided a great deal of contrast to this image, and it can be seen that while a few strands of NiTi were drawn into the stainless steel side of the weld, the two materials remained largely unmixed.

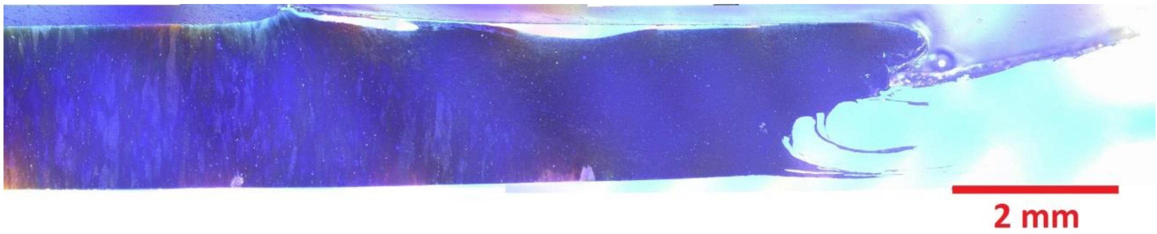

Figure 51: A collage of low-magnification optical microscopy images of the cross-section of Weld 9. The sample was treated with a color tint solution and viewed under polarized light.

This was confirmed by an EDS elemental map, displayed in Figure 52. It can be seen that these two images, created by completely different techniques, correspond very closely.

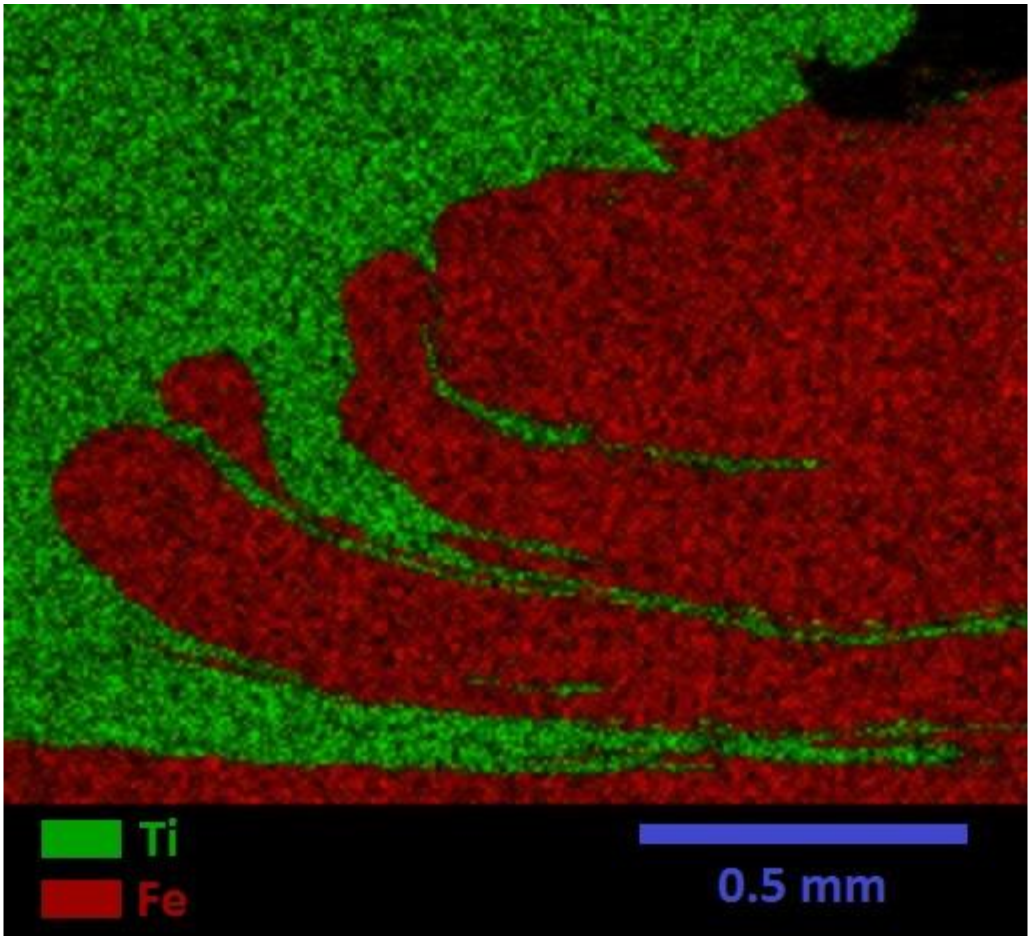

Figure 52: An EDS Map of Weld 9, NiTi-stainless steel. Titanium and iron are shown in green and red, respectively.

An EDS linescan was performed at the interface between NiTi and stainless steel at the location indicated by the red line in Figure 53.

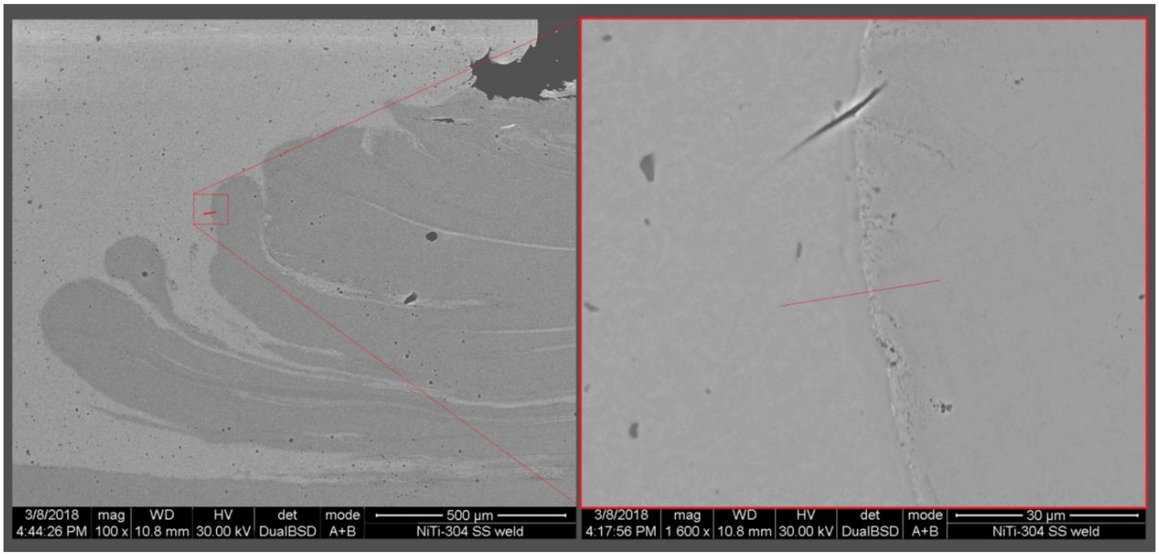

Figure 53: The location of the EDS linescan (depicted by red line) on the cross-section of Weld 9.

The results of the EDS linescan, presented in Figure 54, indicate that the diffusion zone between NiTi and stainless steel is approximately 5 µm wide. However, it should be stressed that this is approaching the spatial resolution limits of the EDS system, so although an upper limit of 5 µm can be drawn on the diffusion zone width, the zone could in fact be much smaller.

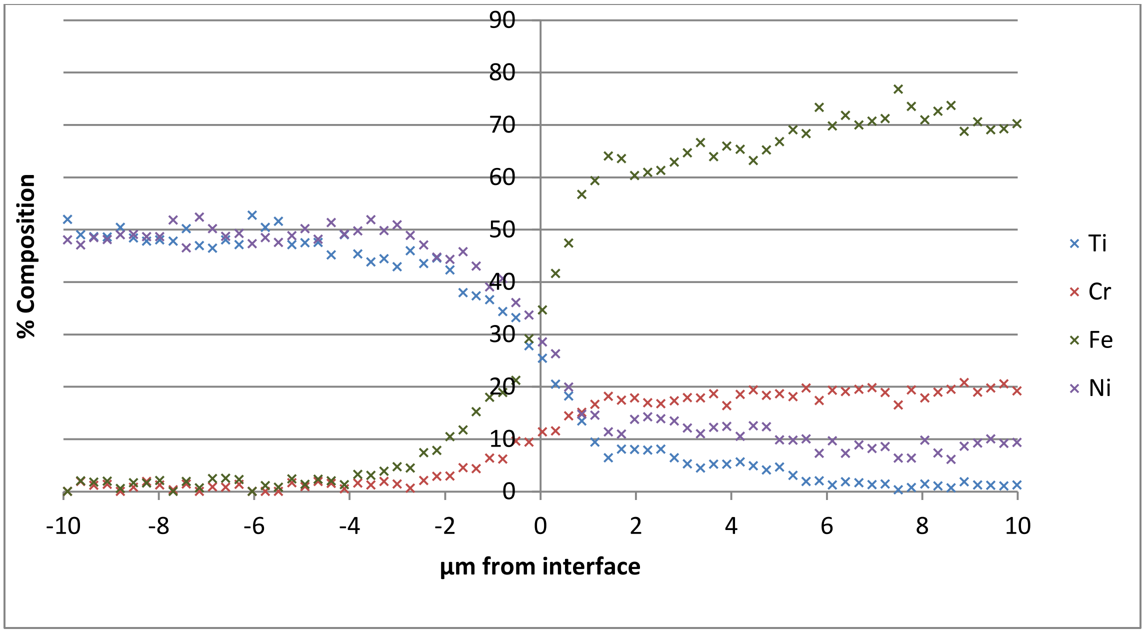

Figure 54: The results of the EDS linescan on NiTi-stainless steel interface in Weld 9.

After the cross-section of Weld 9 was repolished, the stainless steel side was masked off with Scotch tape and the NiTi side was tint etched again. The resulting microstructure is shown in Figure 55.

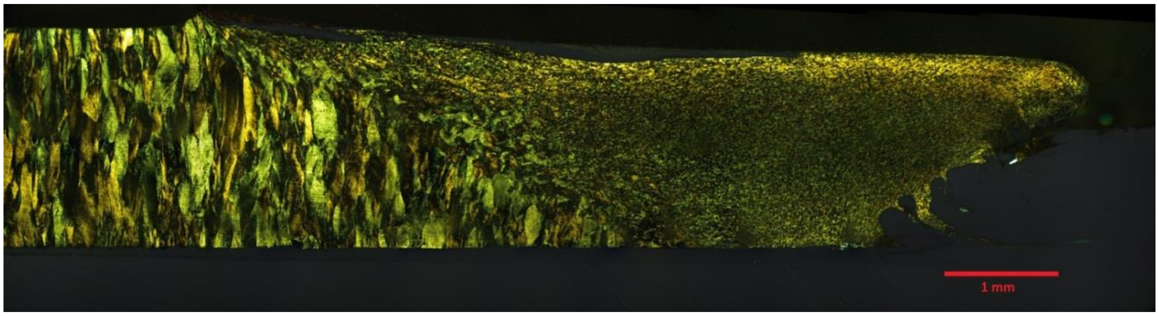

Figure 55: A collage of low-magnification microscopy images of the NiTi side of Weld 9, viewed under polarized light. The NiTi side of the weld was treated with a color-tint solution.

A more detailed view of the SZ can be seen in Figure 56. The mean grain size within the stir zone, measured using the Heyn Lineal Intercept Method, was found to be approximately 8 μm. This is much smaller than the base metal grains, which measured about 125 μm wide and more than 1 mm in length. It is also significantly smaller than the grain size of 20 μm seen in the stir zone of similar NiTi-NiTi friction stir welds performed with the exact same welding parameters.

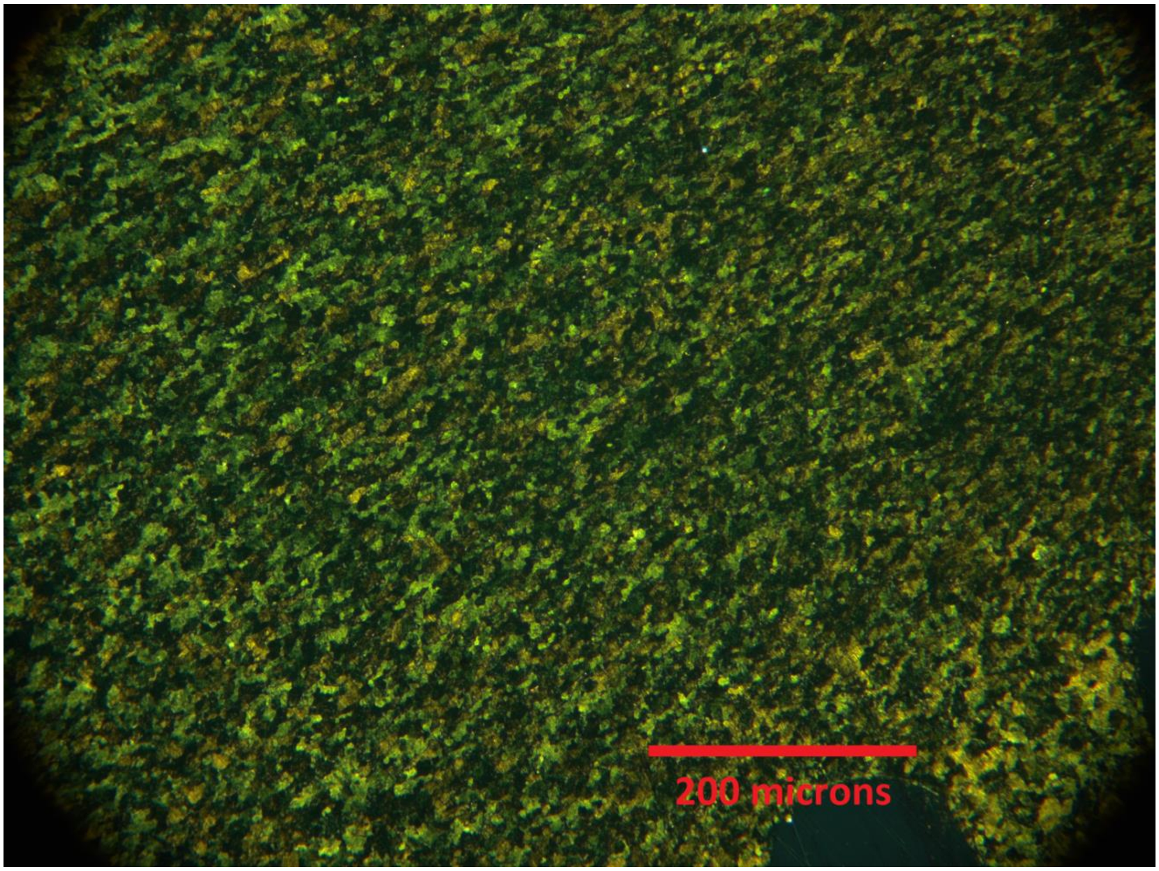

Figure 56: An optical micrograph of the NiTi side of the SZ of Weld 9, tint etched and viewed under polarized light. The average grain size was found to be approximately 8 μm.

Although it was not subjected to in-depth characterization, Weld 12, a dissimilar weld between NiTi and 304 stainless steel at 500 rpm and 40 mm/min, was cross-sectioned and polished in the (mostly) defect-free region near the start of the weld. This cross-section can be seen in Figure 57.

Figure 57: A collage of low-magnification optical microscopy images of Weld 12. NiTi is on the advancing (right) side. Circled are a void near the weld root and a hook defect.

It can be seen that significantly more mixing has taken place in Weld 12 than in Weld 9. The beginning of a hook defect is visible on the advancing side of the weld, while a small void can be observed in the weld root.

Differential Scanning Calorimetry

The DSC curve from the sample in the center of the weld, seen in Figure 58, confirmed that the transformation temperatures did not experience much change. Since the transformation temperatures stayed well above zero, subsequent DSC samples were only cycled down to -50°C, instead of -150°C.

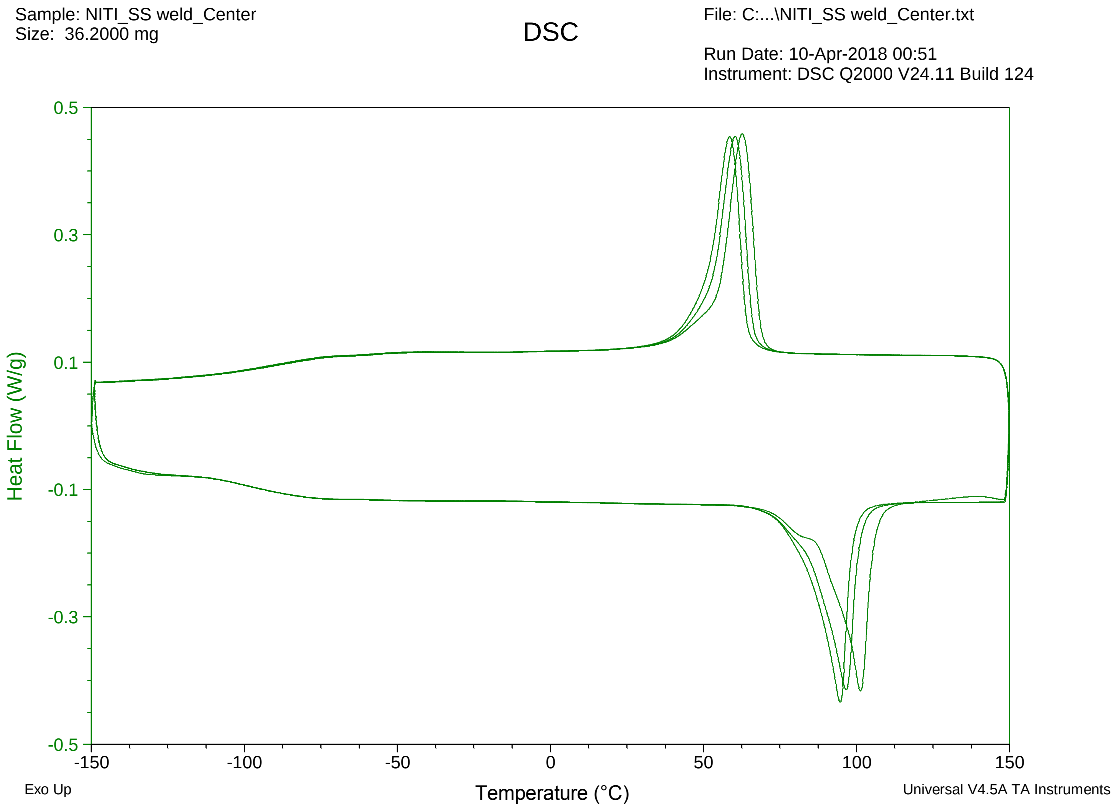

Figure 58: The DSC results for the sample taken from the SZ of Weld 9 on the NiTi side.

The 2nd cycle transformation temperatures, as measured from DSC specimens cut in locations ranging from 20 mm from the weld on the retreating (NiTi) side all the way to the center of the weld, can be seen in Figure 59. The dotted lines represent the transformation temperatures measured from a sample cut from the base metal. Although the A_s and M_s temperatures across the weld correspond well to those measured in the base metal, the A_f temperatures across the weld were three to five degrees lower than in the base metal, and the M_f temperatures across the weld were four to nine degrees higher than in the base metal. The base metal DSC sample was cut from the original NiTi bar in a different location than the sheet used in Weld 9 was cut from, so it was suspected that there might have been some variation in the transformation temperatures throughout the bar. When a second DSC sample was cut from the base metal in a different location to test the homogeneity of the bar, it was found to have transformation temperatures that were around 4 degrees different than the first base metal sample. This indicates that there was some variation in transformation temperatures throughout the bar. Because of this, it may be more appropriate to judge the changes in transformation temperatures caused by the welding process by comparing the transformation temperatures near the weld to those measured in the welded specimen 20 mm away from the weld line. When this is done, the transformation temperatures are seen to exhibit a variation of 3-4°C throughout the welded specimen.

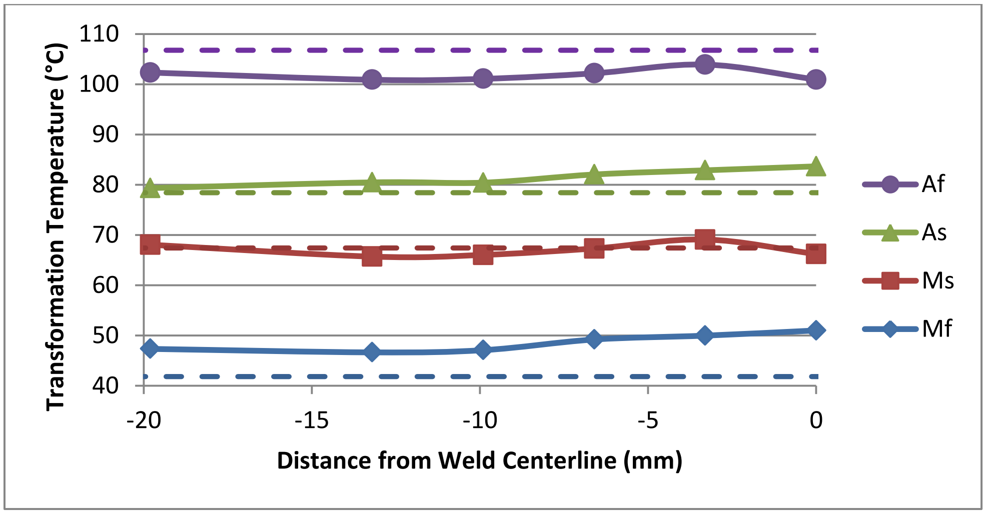

Figure 59: The transformation temperatures taken from DSC results across the NiTi side of Weld 9. The dashed lines represent the corresponding values for the base metal.

Tensile Response of the Welded Material

The first tensile specimen cut from NiTi-stainless Weld 9 was made by removing the top millimeter of the weld to eliminate the deep channel left in the weld, but the backing strip was left attached. This was done because, as explained earlier, the backing strip was unintentionally lap welded to the workpieces during the welding process, but this could also be done intentionally, if a particular design requires a combination of lap and butt welds. The specimen was tensile tested at room temperature (RT), and the resulting stress-strain diagram can be seen in Figure 60.

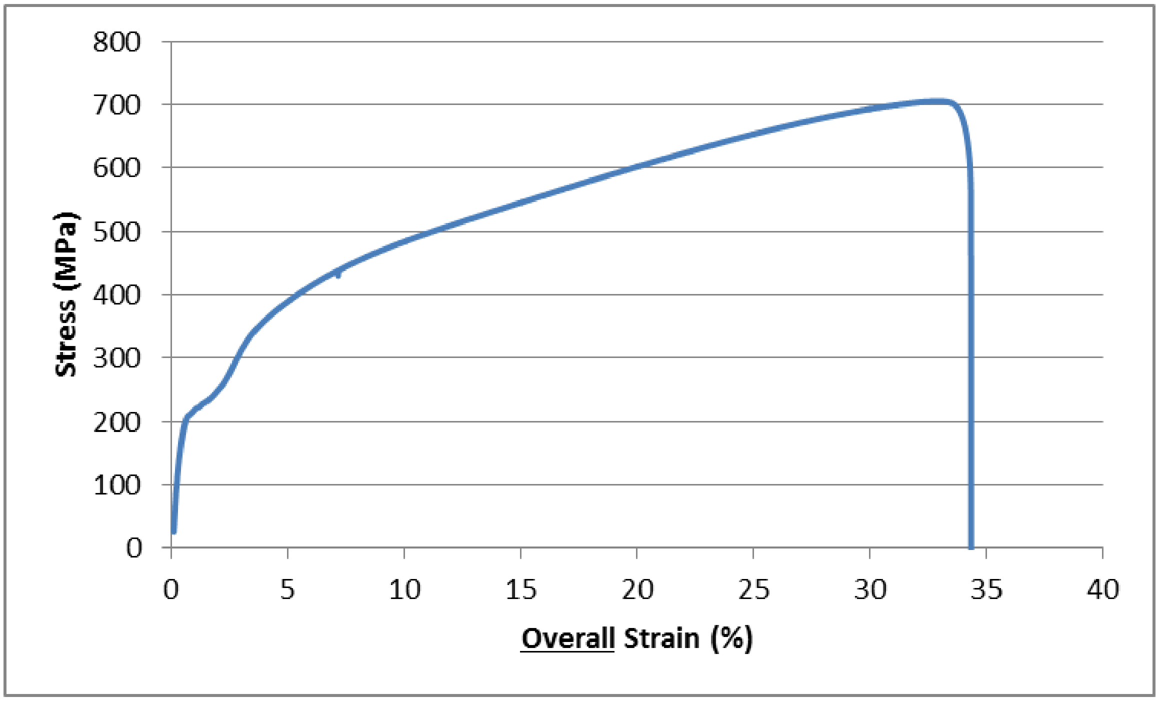

Figure 60: The stress-strain diagram from the ambient temperature tensile test of Weld 9 with the backing strip attached.

The UTS of the specimen was found to be 705 MPa, and the sample failed in the base metal on the stainless steel side, as seen in Figure 61. The strain was measured by a laser extensometer, with two pieces of reflecting tape attached near the ends of the reduced section. The strain to failure was measured at 34%.

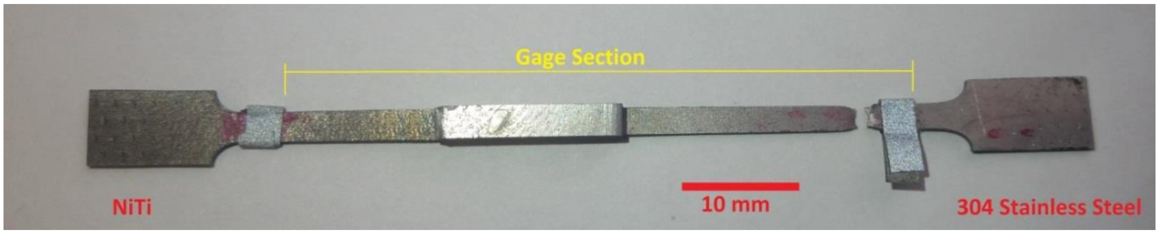

Figure 61: A view of the Weld 9 room temperature tensile specimen with the backing strip attached, after failure.

The stress-strain curve of this specimen is plotted alongside the stress-strain curves of the NiTi base metal and stainless steel base metal in Figure 62. It can be seen that the specimen behaves as a composite rod of two materials connected in series.

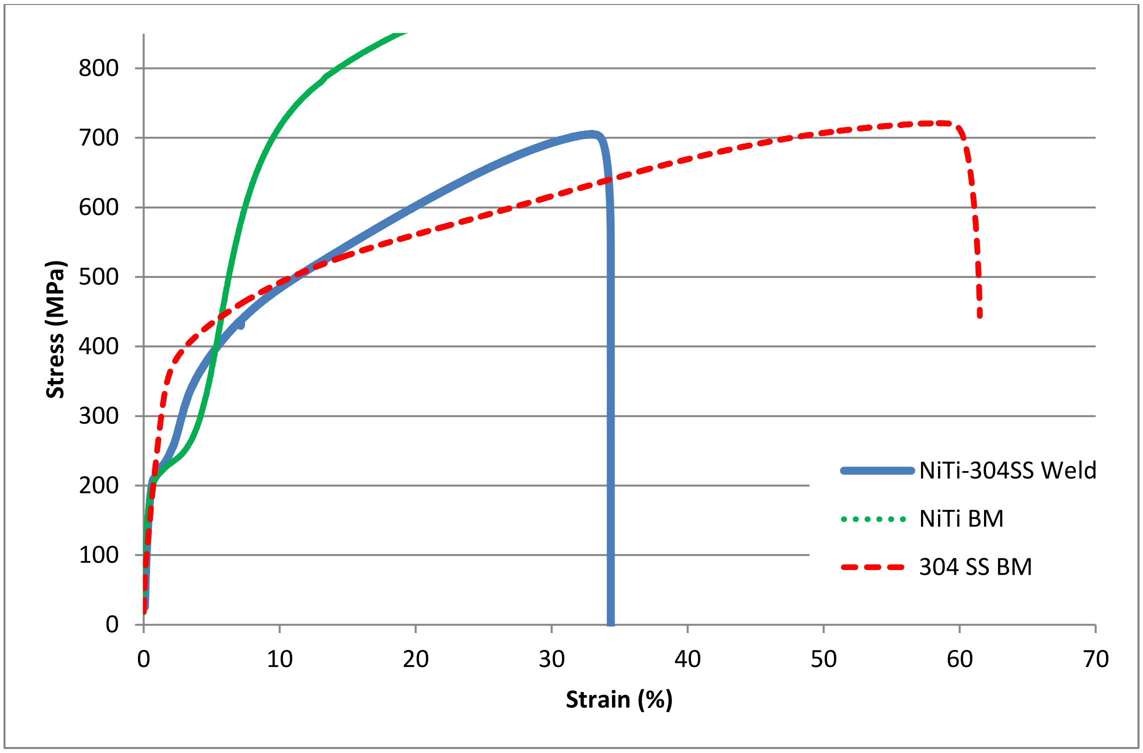

Figure 62: Plot of the stress-strain curve of the Weld 9 room temperature tensile specimen with backing strip attached. The stress-strain curves of the NiTi base metal and stainless steel base metal are also plotted for reference.

A second room temperature tensile test was conducted, this time on a tensile specimen with the backing plate removed. This specimen failed within the weld at a stress of 567 MPa, giving a joint efficiency of 80%. For this test, a laser extensometer was set up to measure the strain in three different regions simultaneously. This allowed the strain in the weld region to be compared to the strain outside of the weld within the NiTi and stainless steel base metal portions of the specimen, as illustrated in Figure 63.

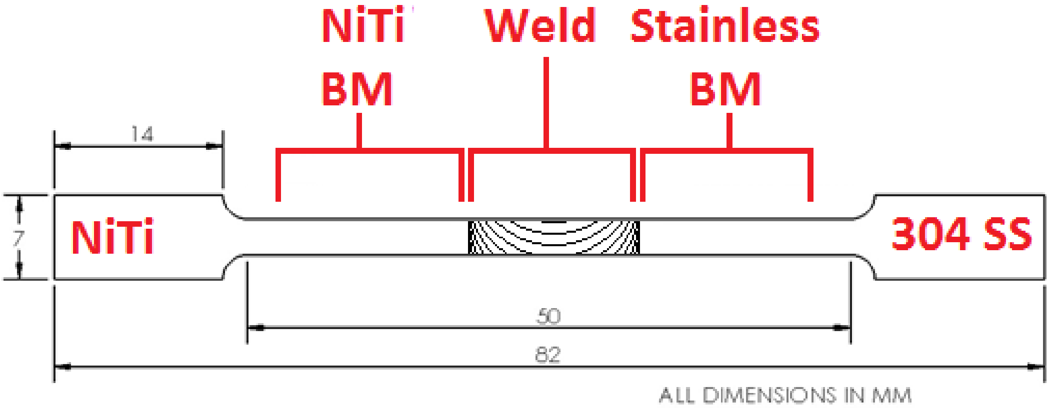

Figure 63: Schematic of gage lengths measured by multi-segment laser extensometer for NiTi-stainless steel Weld 9 tensile tests.

Prior to testing, the thickness was measured all along each tensile specimen. The thickness of each specimen was found to vary by 0.02 mm, so the tensile stress was calculated independently for all three regions measured by the laser extensometer – the NiTi base metal, the weld zone, and the stainless steel base metal. The resulting stress-strain curves for the three regions of the specimen can be seen in Figure 64. It should be noted that some correction was applied to the measured laser extensometer data because spurious reflections caused problems with the laser extensometer readings in all tests conducted this way. In the tensile test reported in Figure 64, this problem occurred when the stress was between 250 and 350 MPa, and then corrected itself. The erroneous data points reported by the extensometer have been replaced by a straight line interpolation for clarity.

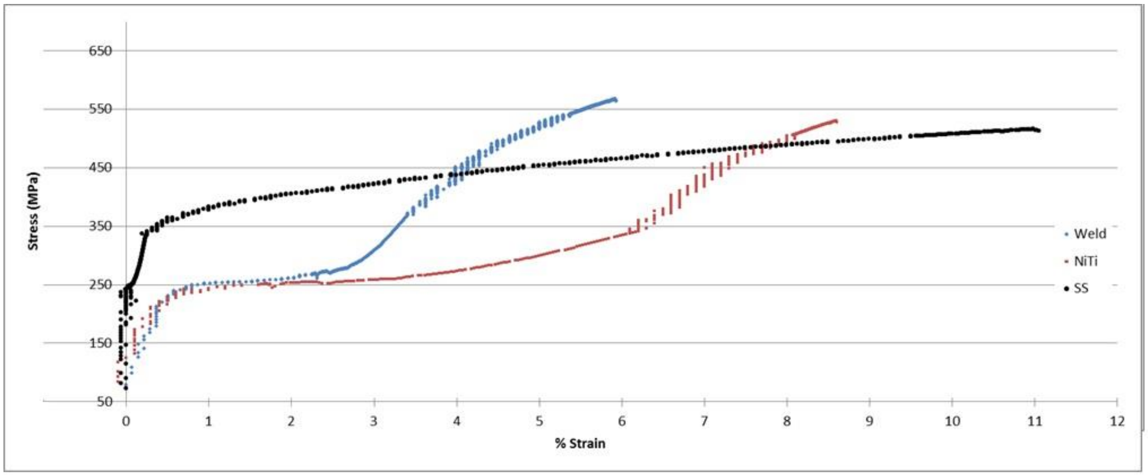

Figure 64: Stress-strain diagrams from a room temperature tensile test of Weld 9 with the backing strip removed. The strain was simultaneously recorded in the weld zone, in the base metal on the NiTi side, and in the base metal on the stainless steel side.

Elevated temperature tensile tests were also conducted on Weld 9 with the backing strip removed so that the NiTi would be in its austenite phase at the beginning of the test. This high temperature (HT) test was conducted at 121°C, approximately 20°C above the A_f temperature measured in the weld. Just as in the previous tensile test, a laser extensometer was used to measure the strain in three different gage lengths of this specimen as well. However, the data recorded from the laser extensometer was unintelligible, most likely due to spurious reflections from the specimen, the shiny inside surface of the environment chamber, and the glass front of the chamber. Therefore, the strain for this test was simply calculated from the crosshead displacement. This is not the most accurate method for calculating strain, but it is considered to be an acceptable method for this case, since the failure strain is not very useful when testing a joint between dissimilar metals. The failure stress is of much more interest in this test, and since the load cell performed correctly, the stress values are valid. The stress-strain diagram of the Weld 9 HT tensile test is presented in Figure 65.

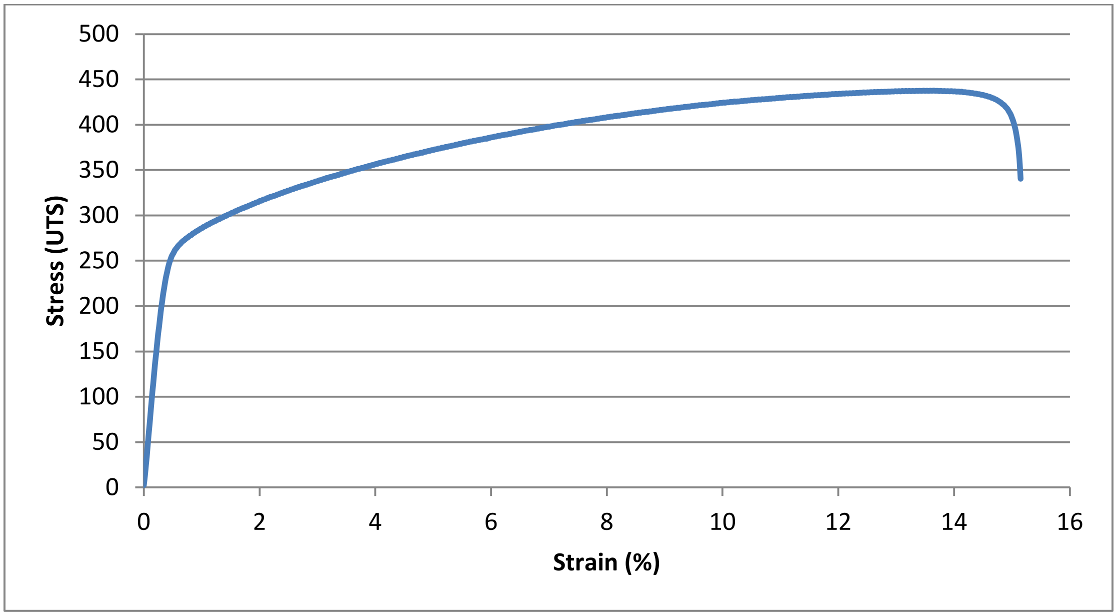

Figure 65: The stress-strain diagram from the high temperature tensile test of Weld 9. The strain values were calculated from the crosshead displacement.

Of even more interest than the failure stress in this case, however, is the failure point in the tensile specimen. As shown in Figure 66, the specimen failed in the base metal on the stainless steel side, around 20 mm from the center of the weld. This indicates that at 121°C, the strength of the joint is greater than the strength of 304 stainless steel, resulting in a weld efficiency of 100%. It should be noted that the failure stress of 437 MPa seems low for 304 stainless steel, but this is because the test was conducted at high temperatures. Additionally, a failure strain of 15.5% seems low for stainless steel, but it should be emphasized that this was the combined strain of the stainless side, the NiTi side (which would most likely only experience 2% strain at this stress and temperature), and the weld region, which typically exhibits increased strain hardening due to grain refinement.
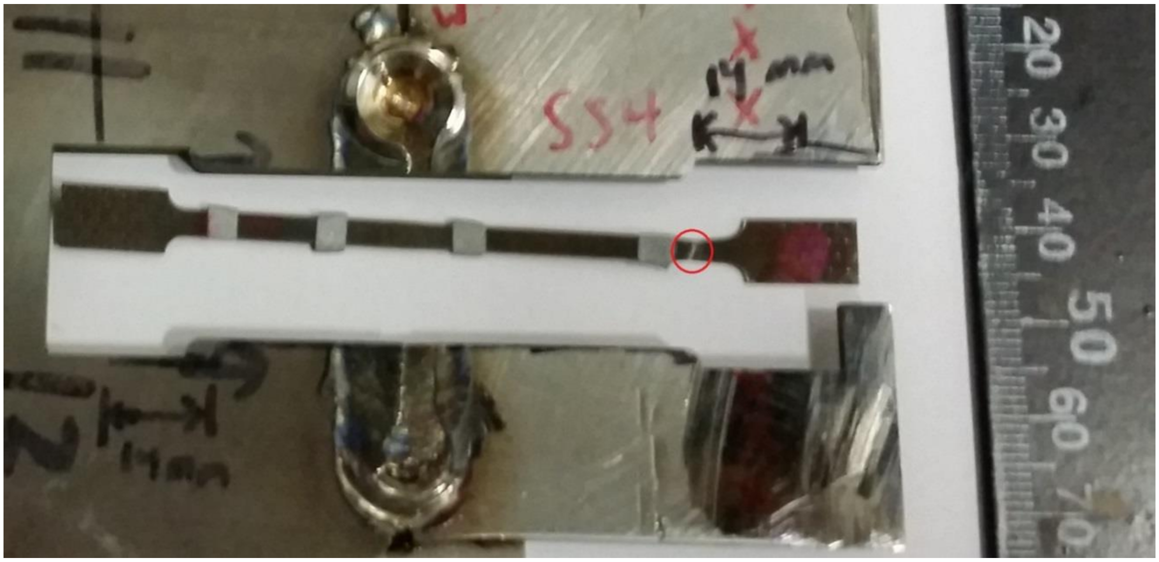
Figure 66: A view of the Weld 9 high temperature tensile specimen, showing where it was cut from in Weld 9. The fracture location of the tensile specimen is circled in red.

Microhardness

The hardness values across the cross-section of Weld 9 are reported in Figure 67, where the NiTi (retreating) side of the weld is on the left and the stainless steel (advancing) side is on the right. When compared to hardness profiles conducted on cross-sections of NiTi-NiTi similar friction stir welds, Weld 9 exhibits surprisingly little scatter in the hardness measurements of NiTi far from the weld. There is a large spike in the hardness near the center of the weld. This could be attributed to grain refinement caused by the stirring in this region, residual stresses present, hard intermetallic phases formed between the NiTi and stainless, or all of the above. However, even this region of high hardness in the center of the weld is not any higher than what has been seen in the stir zone of previous NiTi-NiTi similar friction stir welds, and is much lower than the hardness of 950 HV reported in the middle of laser-welded NiTi-stainless steel joints [4].

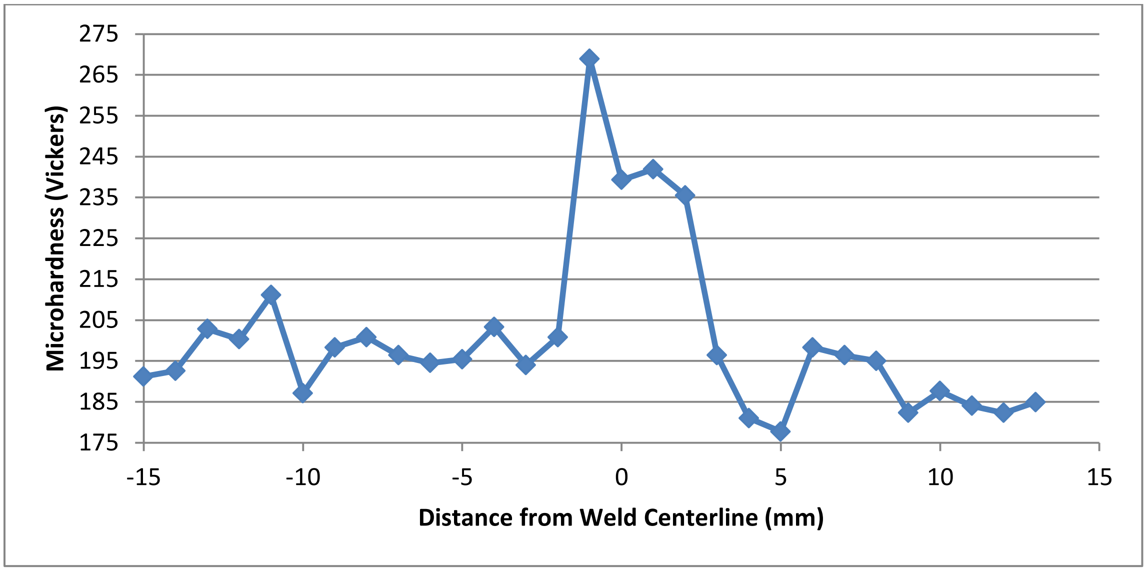

Figure 67: The microhardness profile of Weld 9, measured 1.5 mm below the surface. The advancing (stainless steel) side of the weld is on the right, and the retreating (NiTi) side on the left.

Discussion

It is quite interesting, and initially counterintuitive, that the best dissimilar welds to NiTi were not made by welding to a nickel or titanium based alloy, but rather a steel based alloy. It was expected that introducing a third major element (iron) into the mix would just complicate things further. However, it appears that, at least in this case, similarities in thermal and mechanical properties are more important than chemical similarities. Inconel 625 and Ti-6Al-4V both have extremely low thermal conductivities, less than half of the conductivity of NiTi. 304 stainless steel, on the other hand, has a thermal conductivity (and diffusivity) that is within 10% of that of NiTi.

As far as mechanical properties go, the service temperature of Inconel 625 extends beyond 80% of its absolute melting temperature, which is around the temperature that is reached during FSW [13, 20]. Since it retains so much strength even at these high temperatures, more torque is required to rotate the tool, and more heat is generated. In dissimilar FSW, this means that the majority of the heat will be generated on the Inconel side of the weld. Since Inconel also has a much lower thermal conductivity than NiTi, heat can be expected to build up more on the Inconel side, resulting in a large temperature imbalance. Welding NiTi to Inconel 625 bears some similarities to friction stir welding aluminum alloys to steel, such as the large conductivity difference and the large strength difference at elevated temperatures. Therefore, methods used for friction stir welding aluminum alloys to steel could be adapted to welding NiTi to Inconel 625. This typically involves matching the angle of the aluminum-steel interface with the angle of the tool pin, and offsetting the tool so that it only contacts the steel enough to remove the oxide layer from its surface [44]. A schematic of the process can be seen in Figure 68.

Figure 68: Schematic of effective method of friction stir welding aluminum alloys to steel. The black outline depicts the tool.

Although the welding parameters were not optimized to produce defect-free welds in the steady-state region, some welds were found to have defect-free portions near the start, before temperatures stabilized. The location of these regions provides a hint as to the parameters required for defect-free welds. Since the beginning of Weld 9 was good, but a channel opened up as the weld progressed, it can be inferred that optimal welding conditions were observed at a slightly lower temperature than what was seen in steady-state.

At first glance, the tensile test of Weld 9 with the backing strip attached seems like an “unfair” test, since of course leaving additional material attached to the weld will increase its load-bearing capacity. However, such permanent backing strips are seen in real-world applications, and the joint can almost be considered a hybrid between a butt weld and a lap weld. A similar joint geometry, which could be beneficial when joining materials of different strengths such as these, is depicted in Figure 69. In this embodiment, the weaker material would have a rabbet machined into its surface, into which the stronger material would be inserted. Propellant tanks for European Space Agency rockets include a similar joint geometry, referred to as a J-type joint. In this instance, this is done so that the inside of the Ti-6Al-4V tank will not be contaminated by the weld [24]. In the case of a tank with three welds, the use of a J-type joint is estimated to only increase the empty mass of the propellant tank by 1-2%.

Figure 69: One possible joint configuration, a butt-lap hybrid joint, with the stronger alloy resting in a rabbet cut in the weaker material.

Even though the room temperature tensile test of the NiTi-stainless steel weld without a backing strip failed within the weld, it had an ultimate tensile strength of 567 MPa, which compares favorably with the reported 450 MPa UTS of laser-welded NiTi-stainless steel joints [10]. Laser-welded joints between Ni50.8Ti and 304 stainless steel were seen to fail as the stress increased near the end of the superelastic plateau (which occurred at 450 MPa in Ni50.8Ti), as voids at the interface propagated as the strain increased [45].

When the cross-sections of Weld 9 and Weld 12 are compared, it is clear that there is much more mixing in Weld 12. This is because the welding pitch, measured in mm of translation per rotation, of Weld 12 is less than half of that seen in Weld 9. This means that the material has much more time to be mixed before the tool has passed. This would be expected to improve the bonding between the NiTi and stainless steel, but may compromise the shape-memory properties of the material within the stir zone.

Summary

Based on the above results, it can be concluded that:

- Regions of defect-free weld were produced between NiTi and 304 stainless steel, but the welding parameters that will produce defect-free welds in steady-state have not yet been found.
- Using FSW, it is easier to join NiTi to 304 stainless steel than it is to join NiTi to either Inconel 625 or Ti-6Al-4V.
- The bond formed between NiTi SMAs and 304 stainless steel by friction stir welding is quite strong, with a joint efficiency of 80% at room temperature and 100% at elevated temperatures.
- The use of a permanent stainless steel backing strip resulted in a joint efficiency of 100% between NiTi and stainless steel
- A variation in transformation temperatures of no more than 4°C can be seen on the NiTi side of a dissimilar friction stir weld between NiTi and 304 stainless steel.
- The average microhardness seen in the stir zone of a NiTi-stainless steel weld is 246 HV, compared to 288 HV in the stainless steel base metal and 298 in the NiTi base metal.

CHAPTER IV

SUMMARY OF WORK AND CONCLUSIONS

Based on the results of this study, FSW of NiTi appears technologically feasible apart from the challenges of tool wear and life that are holding back the entire high temperature friction stir welding industry. The identification of tungsten particles in the weld leads to two questions that could dictate the feasibility of using FSW to join NiTi.

The first question, one of pure engineering, relates to the fatigue strength of the joint. Tensile tests in the present study have already demonstrated that the tungsten particles do not cause much, if any, decrease in the strength of the weld when subjected to a one-time load. However, fatigue response may be adversely impacted; therefore, fatigue testing of optimized NiTi-NiTi welds is needed. Up to 90% of mechanical failures are attributed to fatigue [46], so this is a valid concern, particularly for a material commonly used in actuators that can experience hundreds of thousands of cycles. On one hand, an inherent weakness in SMAs themselves could render a reduction in fatigue strength at the weld a moot point, to some extent. This is because NiTi SMAs tend to accumulate irrecoverable strain over thousands of cycles, resulting in functional fatigue, a reduction of their shape memory capabilities [47]. Even if the presence of tungsten particles in the weld does decrease the fatigue life of the joint, this may not pose a problem as long as the fatigue of the welded joint outlasts the functional fatigue of the SMA itself. Of course, in such analysis, failure modes must also be taken into account, since the result of a fracture in the weld may be much more catastrophic than the result of a slow reduction in the work output of the SMA.

The second question that arises from the observation of tungsten particles in the weld is one of tool life, and ultimately, economics. W-Re tools are not cheap, and if a 500 dollar tool can only weld for one meter before it wears out and has to be replaced, then the process is not economical even when compared to laser welding. That is, unless the price of the tool is only a small fraction of the cost of the part being welded. In this case, the shortcomings of NiTi SMAs can once again overshadow a problem seen in FSW. NiTi is very expensive, due to a combination of high purity requirements for raw materials, manufacturing processes, and low production volume. Because of this, the use of expensive FSW tools for welding NiTi is still economically feasible, since the tool cost would only be a small portion of the overall cost of a part made from this high-value material.

Dissimilar FSW of NiTi to 304 stainless steel seems to be promising, but steps will need to be taken to optimize the parameters for the process. The easiest method of friction stir welding NiTi to stainless steel is likely through lap welding. Lap welding has the advantage of only having one material rubbing on the shoulder of the tool, resulting in a more symmetrical process than what is seen with dissimilar butt joints. In fact, NiTi was successfully lap welded to manganese steel, stainless steel, and Ti-6Al-4V in this study, even when friction stir processing was conducted, although the strengths were not measured since lap welding was not investigated in this study. The ease with which lap welds can be made between NiTi and dissimilar alloys warrants their further investigation.

Although it may be easier to obtain a defect-free joint in lap welding, it appears that the parameters for a full defect-free NiTi-stainless butt weld are close at hand, based off of the results of the welds performed in this study. Stationary shoulder friction stir welding (SSFSW) [48] and friction stir spot welding (FSSW) [49] provide other potentially effective methods of joining NiTi to stainless steel.

Major conclusions that were discovered during this study can be summarized by the following:

- NiTi SMAs can be effectively friction stir welded over a wide range of processing parameters, ranging from 300 to 500 rpm at a feed rate of 75 mm/min.
- NiTi-NiTi FSW can result in weld efficiencies of 93% at up to 20% elongation when tested at room temperature, and 84% at up to 7% elongation when tested at high temperature.
- In both room temperature and high temperature tensile tests of NiTi-NiTi welds, the fracture surfaces were observed to be ductile in nature.
- Small changes (less than 7°C) of transformation temperatures were observed as a result of similar FSW of NiTi.
- No distinction could be made between the TMAZ and the SZ in similar FSW of NiTi, but grain refinement in the SZ of similar FSW of NiTi resulted in a mean grain size of 20 µm for a weld conducted at a rotational speed of 400 rpm and a feed rate of 75 mm/min. This is much smaller than the 125 µm wide and 1000 µm long grains seen in the base metal, and was found to increase the strain hardening rate within the weld.
- Large amounts of scatter were seen in the hardness of the NiTi-NiTi samples even outside of the weld. This scatter was not seen in the NiTi-stainless steel weld, and it is suspected to be a result of residual stresses developed due to the fixturing conditions used in the NiTi-NiTi welds.
- Some tool wear was seen in NiTi-NiTi welds, which may adversely affect the fatigue life of the joint. This would need to be thoroughly investigated before the process is impelemented.
- Dissimilar FSW of NiTi to Inconel 625 was not successful due to the large difference in the strengths of the two materials at high temperature. An approach using a toolpath offset from the joint may be necessary to produce quality welds between NiTi and Inconel 625.

- Dissimilar FSW of NiTi to Ti-6Al-4V was not successful, although it is likely that better results could be achieved by using different welding parameters or a different joint geometry.

- Dissimilar FSW of NiTi to AISI 304 stainless steel can produce a strong bond between the two materials, with a strength of 567 MPa seen at room temperature, resulting in a weld efficiency of 84%. This compares favorably with other methods used to weld NiTi to stainless steel. At 121°C, the strength of the NiTi-stainless steel joint was seen to exceed the strength of the stainless steel base metal.

- Very little material mixing was observed in the NiTi-stainless steel weld performed at 400 rpm and 75 mm/min; however, this did not seem to negatively impact the strength of the joint. Much more mixing was seen in the NiTi-stainless steel weld performed at 500 rpm and 40 mm/min, due to the lower pitch of the weld.

- Reducing the tilt angle of the tool from 2.5° to 1.5° reduces the downforce needed to fully consolidate a NiTi-stainless steel weld from 25 kN to 15 kN. Optimizing the tilt angle could prove crucial, especially in cases where the maximum downforce that can be provided by the machine is a limiting factor.

- After the FSW process was carried out between NiTi and stainless steel at 400 rpm and 75 mm/min, a variation of only 4°C was seen in the transformation temperatures of the NiTi. Since the transformation temperatures did not drop drastically within the weld, it can be assumed that very little diffusion occurred between the NiTi and the stainless steel.

- The NiTi grain size in the SZ was reduced to 8 µm after dissimilar FSW of NiTi to stainless steel was performed. This was much smaller than what was seen in the stir zone of the NiTi-NiTi weld performed using the same parameters.

- A maximum microhardness of 267 HV was seen in the weld between NiTi and stainless steel, which is much lower than what would be expected if significant quantities of brittle intermetallic compounds were present in the weld.

REFERENCES

1. Buehler, W.J. and F.E. Wang, *A summary of recent research on the nitinol alloys and their potential application in ocean engineering.* Ocean Engineering, 1968. **1**(1): p. 105-120.

2. Akselsen, O., *Joining of shape memory alloys*, in *Shape Memory Alloys*. 2010, InTech.

3. Ikai, A., K. Kimura, and H. Tobushi, *TIG Welding and Shape Memory Effect of TiNi Shape Memory Alloy.* Journal of Intelligent Material Systems and Structures, 1996. **7**(6): p. 646-655.

4. Oliveira, J.P., R.M. Miranda, and F.M. Braz Fernandes, *Welding and Joining of NiTi Shape Memory Alloys: A Review.* Progress in Materials Science, 2017. **88**: p. 412-466.

5. Falvo, A., F.M. Furgiuele, and C. Maletta, *Laser welding of a NiTi alloy: Mechanical and shape memory behaviour.* Materials Science and Engineering: A, 2005. **412**(1-2): p. 235-240.

6. Wang, W., et al., *Effect of laser welding parameters on formation of NiTi shape memory alloy welds.* Advances in Materials Science and Engineering, 2014. **2014**: p. 1-8.

7. Elahinia, M.H., M. Hashemi, M. Tabesh, and S.B. Bhaduri, *Manufacturing and processing of NiTi implants: A review.* Progress in Materials Science, 2012. **57**(5): p. 911-946.

8. Zimmerly, C.A., O.T. Inal, and R.H. Richman, *Explosive welding of a near-equiatomic nickel-titanium alloy to low-carbon steel.* Materials Science and Engineering: A, 1994. **188**(1): p. 251-254.

9. Meyers, M., *Shock waves and high-strain-rate phenomena in metals: concepts and applications*. 1981: Springer US.

10. Vannod, J., et al., *Mechanical and microstructural integrity of nickel–titanium and stainless steel laser joined wires.* Acta Materialia, 2011. **59**(17): p. 6538-6546.

11. Massalski, T.B., H. Okamoto, P.R. Subramanian, and L. Kacprzak, *Binary alloy phase diagrams. vol. 3.* ASM International, 1990: p. 1485.

12. Mishra, R.S. and Z.Y. Ma, *Friction stir welding and processing.* Materials Science and Engineering: R: Reports, 2005. **50**(1-2): p. 1-78.

13. Nandan, R., T. Debroy, and H. Bhadeshia, *Recent advances in friction-stir welding – Process, weldment structure and properties.* Progress in Materials Science, 2008. **53**(6): p. 980-1023.

14. Mani Prabu, S.S., et al., *Microstructure, mechanical properties and shape memory behaviour of friction stir welded nitinol.* Materials Science and Engineering: A, 2017. **693**: p. 233-236.

15. Lima, J.S. and A.C. Neto, *Friction stir welding of austenitic NiTi shape memory alloys.* Global Journal of Research In Engineering, 2017.

16. London, B., et al., *Friction stir processing of Nitinol.* Friction Stir Welding and Processing III, 2005: p. 67-74.

17. Barcellona, A., et al., *Friction stir processing of NiTi shape memory alloy: microstructural characterization.* International Journal of Material Forming, 2010. **3**(S1): p. 1047-1050.

18. Wu, M.H. and L.M. Schetky. *Industrial applications for shape memory alloys*. in *International conference on shape memory and superelastic technologie*. 2000. Pacific Grove, California.

19. Chau, E.T., *Comparative study of joining methods for a SMART aerospace application,* in *School of Applied Sciences*. 2007, Cranfield University.

20. *MatWeb Material Property Data*. 2018 April 30, 2018; Available from: http://www.matweb.com/search/DataSheet.aspx?MatGUID=44afc7d3c6eb4829bc2df27884fd2d6c&ckck=1.

21. Garfinkle, M., *Exploratory study of elevated temperature tensile properties of alloys based on the intermetallic compound tini.* Metallurgical Transactions, 1974. **5**(11): p. 2383-2388.

22. Zhou, L., H.J. Liu, and Q.W. Liu, *Effect of rotation speed on microstructure and mechanical properties of Ti–6Al–4V friction stir welded joints.* Materials & Design (1980-2015), 2010. **31**(5): p. 2631-2636.

23. Buffa, G., L. Fratini, F. Micari, and L. Settineri, *On the choice of tool material in friction stir welding of titanium alloys.* Proceedings of NAMRI/SME, 2012. **40**.

24. Brassington, W.D.P. and P.A. Colegrove, *Alternative friction stir welding technology for titanium–6Al–4V propellant tanks within the space industry.* Science and Technology of Welding and Joining, 2017. **22**(4): p. 300-318.

25. Saint-Venant, A.J., *Memoire sur la torsion des prisms.* Mem. div. sav. Acad. Sci, 1856. **14**: p. 233-560.

26. *ASTM E384-17 Standard test method for microindentation hardness of materials*. 2017, ASTM International: West Conshohocken, PA.

27. Bormann, T., et al., *Microstructure of selective laser melted nickel–titanium.* Materials Characterization, 2014. **94**: p. 189-202.

28. Threadgill, P.L., A.J. Leonard, H.R. Shercliff, and P.J. Withers, *Friction stir welding of aluminium alloys.* International Materials Reviews, 2013. **54**(2): p. 49-93.

29. Colegrove, P.A., *Modelling of friction stir welding*, in *Department of Engineering*. 2003.

30. Lagoudas, D.C., *Shape memory alloys: modeling and engineering applications*. 2008: Springer Science & Business Media.

31. Yan, X.J., D.Z. Yang, and X.P. Liu, *Influence of heat treatment on the fatigue life of a laser-welded NiTi alloy wire.* Materials Characterization, 2007. **58**(3): p. 262-266.

32. Imam, M., V. Racherla, and K. Biswas, *Effect of backing plate material in friction stir butt and lap welding of 6063-T4 aluminium alloy.* The International Journal of Advanced Manufacturing Technology, 2014. **77**(9-12): p. 2181-2195.

33. Khaled, T., *An Outsider Looks at Friction Stir Welding*. Vol. 25. 2005.

34. *ASTM E112-13 Standard test method for determining grain size*. 2013, ASTM International: West Conshohocken, PA.

35. Shihab, N.R., T.A. Enab, A.M. Galal, and M.S. Gatas, *Effect of grain size on orange peel in oxygen free copper wire produced by upcast.* International Journal of Scientific and Engineering Research, 2016.

36. Hall, E.O., *The deformation and ageing of mild steel: III discussion of results.* Proceedings of the Physical Society. Section B, 1951. **64**(9): p. 747.

37. Dorbane, A., et al., *Microstructural observations and tensile fracture behavior of FSW twin roll cast AZ31 Mg sheets.* Materials Science and Engineering: A, 2016. **649**: p. 190-200.

38. Kockar, B., et al., *Thermomechanical cyclic response of an ultrafine-grained NiTi shape memory alloy.* Acta Materialia, 2008. **56**(14): p. 3630-3646.

39. Kockar, B., et al., *Effect of severe ausforming via equal channel angular extrusion on the shape memory response of a NiTi alloy.* Journal of Nuclear Materials, 2007. **361**(2-3): p. 298-305.

40. Stirling Company., *Stirling, A Book on Steam for Engineers*. 1905, Chicago: Burrow Company.

41. Song, K.H. and K. Nakata, *Mechanical properties of friction-stir-welded Inconel 625 alloy.* Materials Transactions, 2009. **50**(10): p. 2498-2501.

42. Plaine, A.H. and N.G. Alcântara, *Prediction of friction stir welding defect-free joints of AISI 304 austenitic stainless steel through axial force profile understanding.* Materials Research, 2014. **17**(5): p. 1324-1327.

43. Goo, E. and R. Sinclair, *The B2 to R transformation in Ti50Ni47Fe3 and Ti49. 5Ni50. 5 alloys.* Acta Metallurgica, 1985. **33**(9): p. 1717-1723.

44. Watanabe, T., H. Takayama, and A. Yanagisawa, *Joining of aluminum alloy to steel by friction stir welding.* Journal of Materials Processing Technology, 2006. **178**(1): p. 342-349.

45. Vannod, J., *Laser welding of nickel-titanium and sainless steel wires- processing, metallurgy, and properties*, in *Materials Science*. 2011, École Polytechnique Fédérale De Lausanne. p. 129.

46. Campbell, F.C., *Elements of metallurgy and engineering alloys*. 2008, Materials Park, Ohio :: ASM International.

47. Lagoudas, D.C., et al., *Thermomechanical fatigue of shape memory alloys.* Smart Materials and Structures, 2009. **18**(8).

48. Beckman, A., *Development of stationary shoulder for friction stir welding*. 2014, Chalmers University: Gothenburg, Sweden.

49. Gerlich, A., P. Su, and T.H. North, *Peak temperatures and microstructures in aluminium and magnesium alloy friction stir spot welds.* Science and Technology of Welding and Joining, 2013. **10**(6): p. 647-652.

APPENDIX A

TENSILE TESTS OF NiTi SIMILAR WELDS

The stress-strain diagrams of additional tensile tests of the NiTi similar welds have been included for the sake of completeness. Many of these early tests failed prematurely at the location of the hook defect, but they still exhibit the same trends as the final tests. It should be emphasized that there is some discrepancy in the stress-strain diagrams of the welds. For some tests, the top surface of the specimen was not machined or ground flat, so the specimen was slightly thinner at the location of the weld. Since the ultimate tensile strength of the weld was the main interest, and the specimens were expected to fail at their thinnest location, this thinnest location was used in calculating the stress. For the final tensile test, shown in Chapter II, the top and bottom surfaces of the specimen were machined flat, to obtain a more uniform thickness.

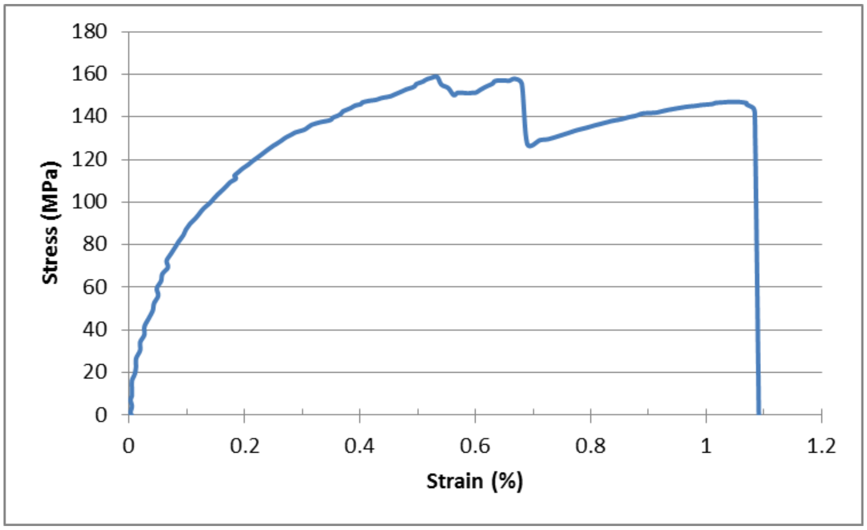

A-1: Stress-strain diagram from first room temperature tensile test of 350 rpm weld. The hook defect was not removed, and a drop in stress can be seen at 0.7% strain as the crack propagated along the defect.

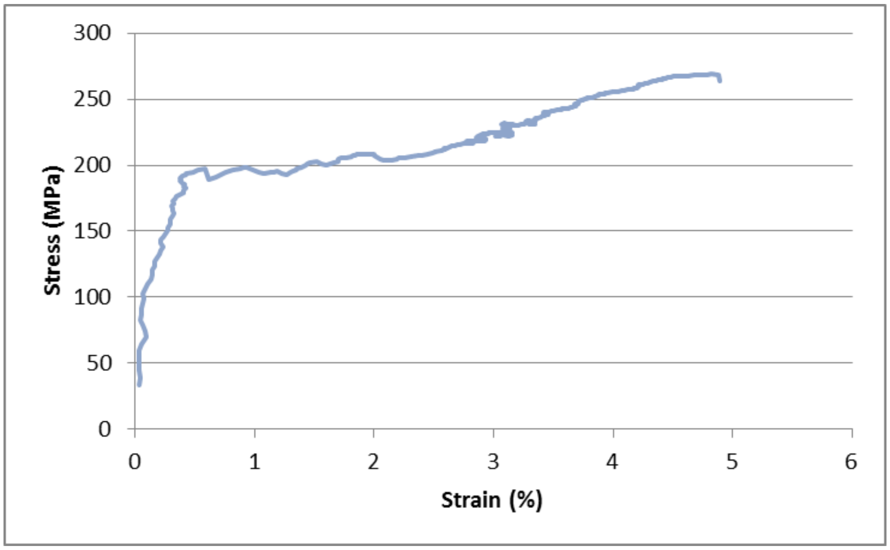

A-2: Stress-strain diagram from a room temperature tensile test of the 400 rpm weld with the hook defect partially removed. The strain was measured with a laser extensometer, and particularly at relatively low strains, the limited resolution of the extensometer is evident.

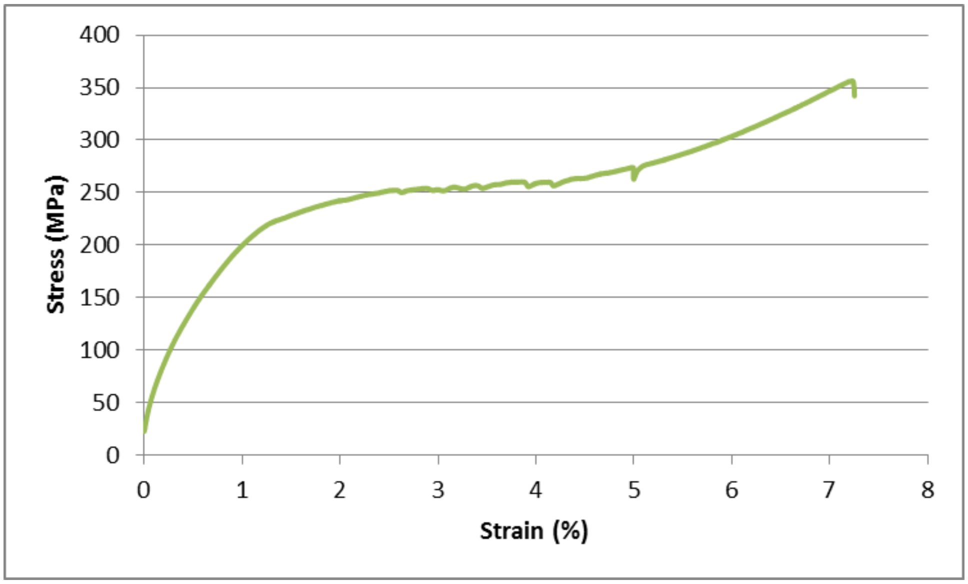

A-3: Stress-strain diagram from a tensile test of a 350 rpm weld specimen that was mechanically ground 0.8 mm to remove the hook defect. However, not all of the defect was removed, and images from Digital Image Correlation revealed that the crack began to open when 2% strain was reached. The crack continued to propagate, as indicated by the small drops evident in the stress-strain curve, before failing at 7.5% strain. The strain in this test was calculated from the crosshead displacement.

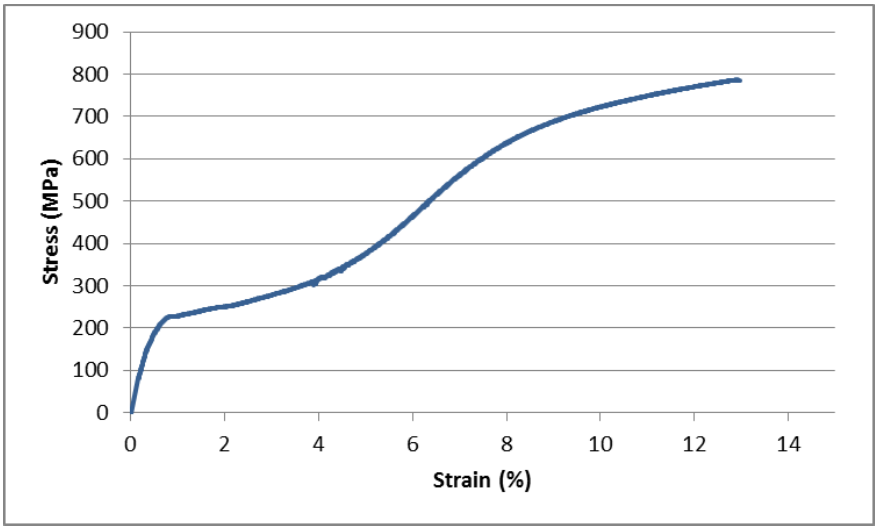

A-4: Stress-strain diagram of a room temperature tensile test of the first 400 rpm weld. The bottom of the specimen was ground away to remove the hook defect, but the top surface of the specimen was not fully ground away to remove the ring pattern left by the tool, so the specimen was not of entirely uniform thickness. The thinnest portion, at the center of the weld, was used to calculate the stress, since it was expected to break in the thinnest spot. This is why the martensitic plateau is not horizontal in the plot.

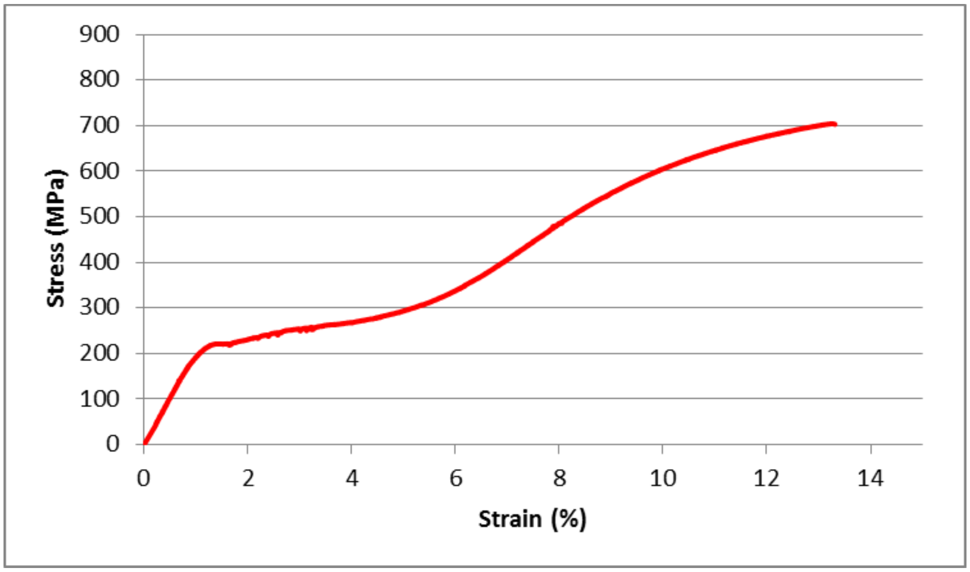

A-5: Stress-strain diagram of a room temperature tensile test of the 450 rpm weld. The strain rate was unintentionally set to $5x10^{-5}$ instead of $5x10^{-4}$. The hook defect was mostly ground away from the bottom of the specimen, but the ring pattern was not ground away from the top, resulting in a slightly non-uniform specimen thickness.

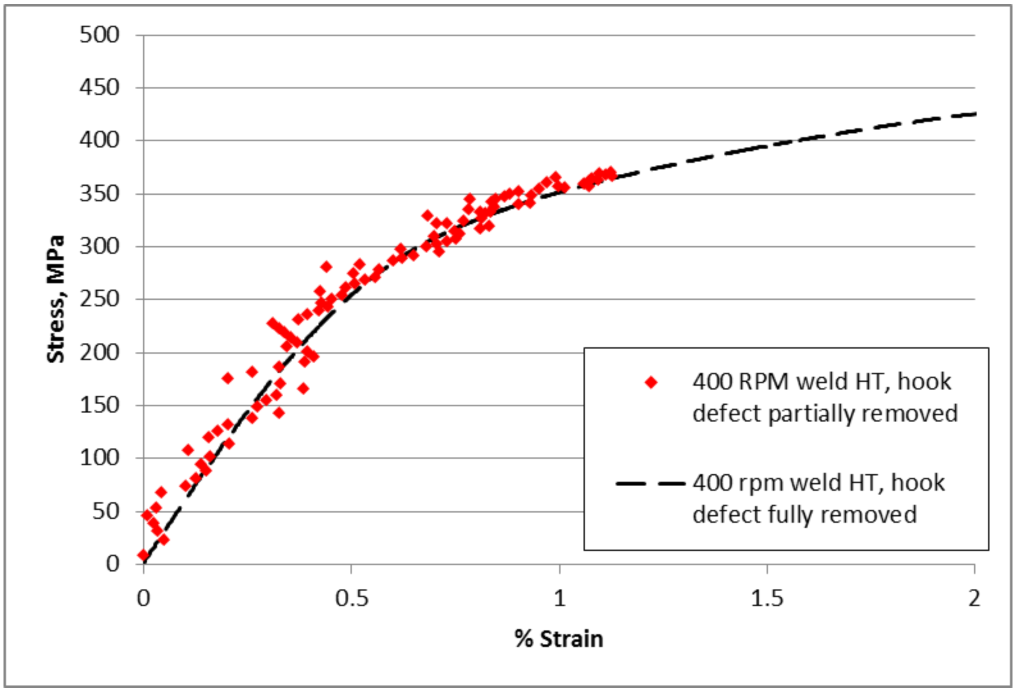

A-6: Stress-strain diagram of a high temperature (129 °C) tensile test of the first 400 rpm weld with the hook defect only partially removed. The bottom of this specimen was machined away in an attempt to remove the hook defect, but not enough material was removed, and a portion of the hook defect remained. The specimen then failed at this location at 1.1% strain. A laser extensometer was used for this test, which resulted in some noise in the strain data. Therefore, the data is plotted as points, rather than a curve. The curve from a high temperature tensile test of second 400 rpm weld is indicated with a dashed line. Although this weld also had a hook defect, the "hook" in this case was made up of NiTi from the backing strip, rather than steel as seen in the first set of welds. This illustrates that the two tests display the same trend, despite the premature failure of the first test. Additionally, it indicates that a hook defect is much more detrimental to strength when it is made up of a dissimilar alloy.

APPENDIX B

ADDITIONAL DSC DATA FOR NiTi SIMILAR WELDS

Additional differential scanning calorimetry curves are presented, with a focus on the unsolved mystery of the double-peak seen in the first cycle DSC heating curve.

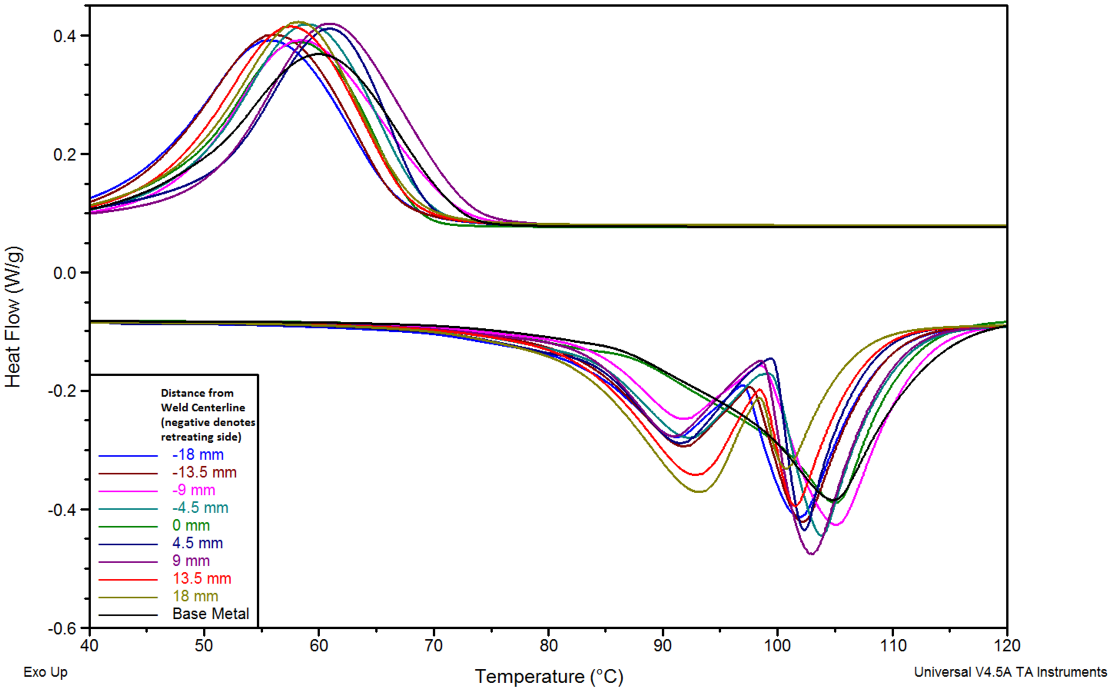

A-7: First cycle DSC results for all samples from 2nd 400 rpm weld.

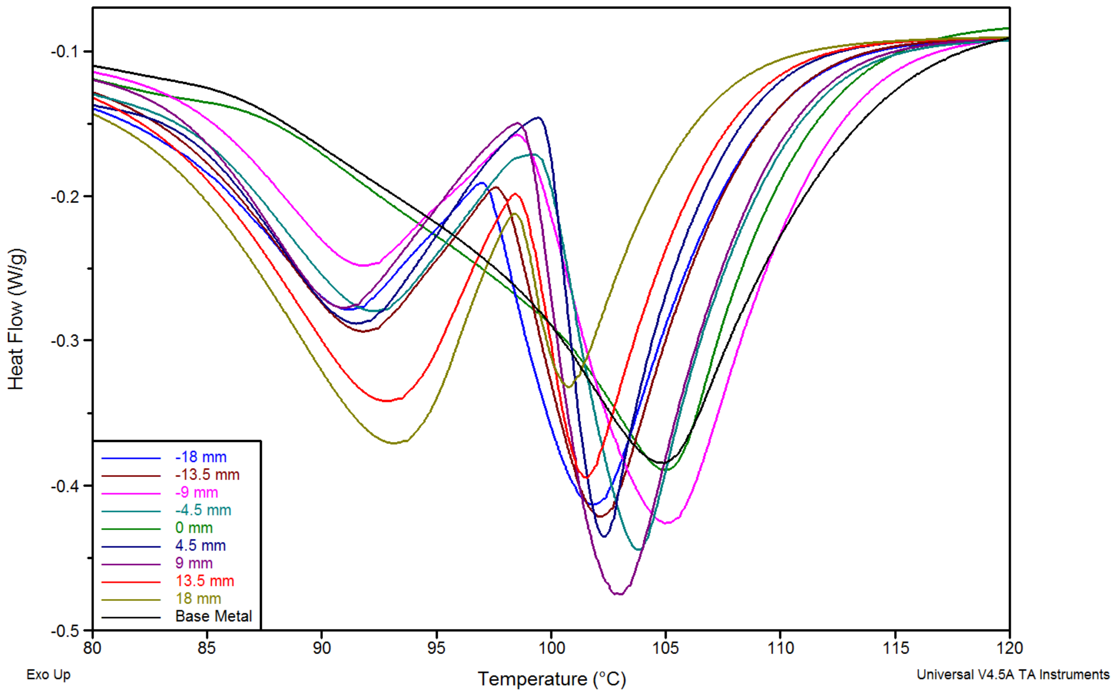

A-8: Magnified view of double-peaks on first cycle DSC curves of samples from second 400 rpm weld.

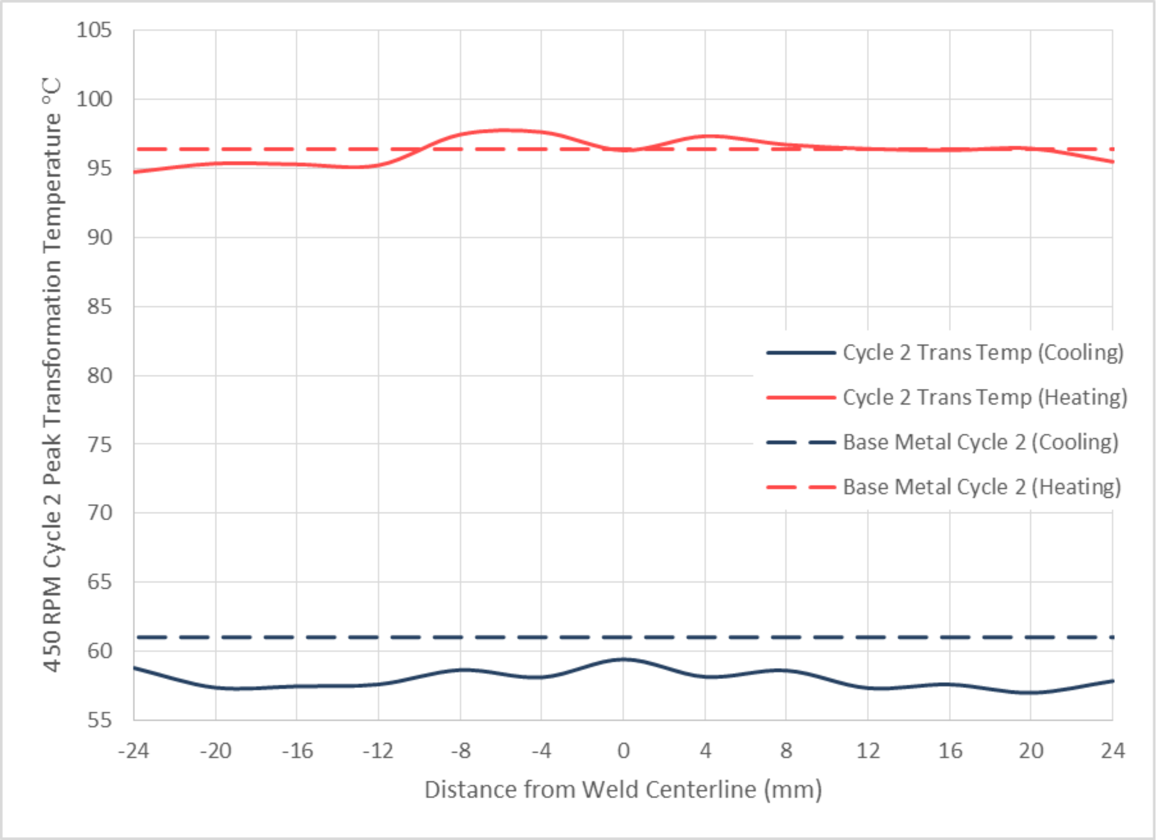

A-9: Peak transformation temperatures from cycle 2 DSC data for 450 rpm weld. The first cycle curves for the 450 rpm weld did not exhibit a double-peak. These specimens were cut with a slow-speed metallurgical saw instead of DSC. However, 400 rpm specimens were also cut with this method and still displayed a double-peak.